Journal of Elasticity
https://doi.org/10.1007/s10659-025-10114-y

RESEARCH

Determination of Diffraction Elastic Constants Using the Maximum Entropy Method

Maximilian Krause[1] · Michael Zürn[2] · Jens Gibmeier[2] · Thomas Böhlke[1]

Received: 9 January 2025 / Accepted: 11 January 2025

Abstract

X-ray diffraction methods are an established technique to analyze residual stresses in polycrystalline materials. Using diffraction, lattice plane distances are measured, from which residual stresses can be calculated by using diffraction elastic constants which can be inferred from experimental measurements or calculated based on micromechanical model assumptions. We consider two different generalizations of existing micromechanical models for the case of texture-free, i.e. statistically isotropic, single-phase polycrystals. The first is based on the singular approximation method of classical micromechanics, from which existing Voigt, Reuss, Hashin-Shtrikman and self-consistent methods are recovered. The second approach, which is newly proposed in this work, is based on the micromechanical Maximum Entropy Method. Both approaches are applied to the problem of calculating diffraction elastic constants of texture-free cubic polycrystals and are found to be consistent with each other in that case. Full-field FFT simulations are used to validate the analytical models by simulating X-ray diffraction measurements of copper. In the simulative setting, many sources of experimental measurement error are not present, which results in a particularly accurate validation of theoretical bounds and approximations. The first core result of the paper is a formulation of diffraction elastic constants for texture-free polycrystals in terms of the macroscopically measurable effective shear modulus. These diffraction elastic constants can be adapted to the properties of a given material sample. The second core result is the validation of the Maximum Entropy Method for X-ray diffraction stress analysis of texture-free single-phase materials as a preliminary step before extending the method to textured and multi-phase materials.

✉ T. Böhlke
thomas.boehlke@kit.edu

M. Krause
maximilian.krause@kit.edu

M. Zürn
michael.zuern@kit.edu

J. Gibmeier
jens.gibmeier@kit.edu

[1] Chair for Continuum Mechanics, Institute of Engineering Mechanics, Karlsruhe Institute of Technology (KIT), Karlsruhe, Germany

[2] Institute for Applied Materials—Materials Science and Engineering, Karlsruhe Institute of Technology (KIT), Karlsruhe, Germany

Keywords Maximum entropy method · Linear thermoelasticity · Heterogeneous materials · Diffraction · Residual stress analysis

Mathematics Subject Classification 74E15 · 74M25 · 74-05

1 Introduction

Diffraction methods are an established technique to analyze residual stresses in polycrystalline materials. By Bragg's Law, information about the lattice strains can be extracted from diffraction measurements using X-rays, synchrotron X radiation or neutron beams to irradiate the material. Since for a given incident angle and wavelength, diffraction only occurs in grains with a particular orientation and lattice plane distance, the information acquired from a single diffraction measurement does not describe the entire polycrystal. Interpreting the measured diffraction data as an overall residual stress therefore requires microstructural assumptions on local strain distributions.

This work focuses on surface stress analysis using X-ray diffraction (XRD) with conventionally generated soft X-rays, which has its origins in the pioneering work by Lester and Aborn [22]. In particular, the $\sin^2(\psi)$ technique proposed by Macherauch and Müller [24] is discussed. This well-established technique is among the most commonly used stress analysis techniques today [10]. While other approaches to XRD stress analysis such as the $\cos(\alpha)$ technique pioneered by Taira and Tanaka [31] are not explicitly discussed, the fundamental micromechanical relations underlying the analysis are the same, and the micromechanical methods described in this work should be applicable.

The relationship between lattice strains, which affect diffraction, and overall residual stresses can, in the texture-free case, be described by diffraction elastic constants (DECs), which can be inferred from experimental measurements or calculated from single-crystal elastic constants. Initially the calculation of DECs was based on the simple micromechanical assumptions due to Voigt [33] and Reuss [28]. A more sophisticated assumption is the self-consistent Eshelby-Kröner approximation formulated by Kröner [19], which was applied to XRD stress analysis by, e.g., Bollenrath et al. [3], and is still widely used today.

The goal of this work is a systematic description of the calculation of DECs from a micromechanical perspective, leading to the application of more recent micromechanical methods to the problem. In addition to classical Eshelby-based approaches, the Maximum Entropy Method (MEM) formulated by Kreher and Pompe [18] is applied to XRD stress analysis for the first time. While this work focuses on texture-free cubic polycrystals to establish the MEM, the MEM is generally applicable to textured and multi-phase polycrystals.

The manuscript is organized as follows. In Sect. 2, elastic constants for X-ray diffraction methods for statistically isotropic cubic polycrystals are re-derived and parametrized by a single macroscopically measurable parameter. Formulas for the well-known Reuss, Voigt, self-consistent and Hashin-Shtrikman approaches are derived as special cases of the singular approximation in Sect. 3. In Sect. 4, the Maximum Entropy Method is introduced as a new approach to the X-ray diffraction method and also simplified for the isotropic case. In Sect. 5, a method to simulate diffraction experiments using FFT full-field solvers is introduced. Analytical methods, simulations and experimental results for DECs are compared in Sect. 6 for the example of fine-grained ferritic steel. In Sect. 7, stress analysis is carried out for copper using analytically calculated DECs. In Sect. 8, the results are summarized.

Notation A symbolic tensor notation is preferred throughout the manuscript. Vectors are written bold ($\boldsymbol{n}$), second-order tensors are bold capital or greek letters ($\boldsymbol{Q}$, $\boldsymbol{\sigma}$) and fourth-order tensors are blackboard bold ($\mathbb{C}$). The dyadic product is denoted $\otimes$. Matrix-vector and matrix-matrix products are written without a symbol ($\boldsymbol{Q}\boldsymbol{n}$, $\boldsymbol{Q}\boldsymbol{A}$, $\mathbb{C}\mathbb{A}$). The application of a fourth-order tensor to a second-order tensor is written $\mathbb{C}[\boldsymbol{\varepsilon}]$. Dot products $\boldsymbol{\sigma} \cdot \boldsymbol{\varepsilon}$ are always scalar products, regardless of tensor order. Rotations of arbitrary objects are denoted via the Rayleigh product $\boldsymbol{Q} \star A$. The spherical-deviatoric split of second-order tensors is written $\boldsymbol{A} = \mathrm{sph}(\boldsymbol{A}) + \mathrm{dev}(\boldsymbol{A})$. The corresponding spherical projector is $\mathbb{P}^{\circ} = \mathbf{1} \otimes \mathbf{1}/3$, or in index notation using Kronecker deltas, $P^{\circ}_{ijkl} = \delta_{ij}\delta_{kl}/3$. The deviatoric projector is $\mathbb{P}' = \mathbb{I}^{\mathrm{S}} - \mathbb{P}^{\circ}$ with the symmetric identity $\mathbb{I}^{\mathrm{S}}$ being defined in index notation as $I^{\mathrm{S}}_{ijkl} = (\delta_{ik}\delta_{jl} + \delta_{il}\delta_{jk})/2$. For fourth-order tensors, matrix-matrix products ($\mathbb{A}\mathbb{B}$), the major transposition ($\mathbb{A}^{\mathrm{T_H}}$), inversions ($\mathbb{A}^{-1}$) and the Moore-Penrose pseudoinverse ($\mathbb{A}^{+}$) are defined by representing these tensors as linear maps on symmetric second order tensors, i.e., using 6 × 6-matrix representations. Angular brackets $\langle \cdot \rangle$ denote statistical averages.

2 XRD Stress Analysis

2.1 The $\sin^2(\psi)$ Technique

The following section summarizes stress analysis using the $\sin^2(\psi)$ technique as described by Noyan and Cohen [27], which is based on diffraction measurements. The phenomenon of diffraction of X-rays at a crystal lattice relies on elastic scattering, which is explained by Bragg's law as depicted in Fig. 1. For a given lattice plane described by the lattice plane normal $\boldsymbol{n}$, diffraction occurs if the angle between lattice plane and incident beam θ, the wavelength λ and the lattice plane distance D satisfy

$$n\lambda = 2D\sin(\theta), \quad n \in \mathbb{N}. \tag{1}$$

The samples considered in this work are polycrystalline, such that multiple randomly oriented grains (crystallites) may be irradiated by the beam. In this work, crystallites are presumed to have approximately perfect lattices without twinning, plastic strain gradients or other heterogeneities, such that the lattice orientation is constant in a single crystallite. The crystallite orientation can be described by a second-order orientation tensor $\boldsymbol{Q} \in Orth^{+}$. In the cubic case,

$$\boldsymbol{g}_i = \boldsymbol{Q}\boldsymbol{e}_i \tag{2}$$

yields the normalized lattice basis vectors, which form an orthonormal coordinate system.

In Fig. 1, diffraction is shown schematically for a simplified example lattice in a 2D projection. Depending on the crystal structure, diffraction can occur on various differently oriented lattice planes. For a given lattice plane specified by Miller indices (hkl), the lattice plane normal vector is given in the normalized crystal coordinate system $\boldsymbol{g}_i$ as

$$\boldsymbol{n}((hkl), \boldsymbol{Q}) = \frac{h\boldsymbol{g}_1 + k\boldsymbol{g}_2 + l\boldsymbol{g}_3}{\sqrt{h^2 + k^2 + l^2}}. \tag{3}$$

As it is not possible to crystallographically distinguish the (hkl) plane with crystallographically equivalent planes such as the (klh) plane, a more precise definition of $\boldsymbol{n}$ is based on the set of all crystallographically equivalent lattice planes $\{hkl\}$, called the family of lattice

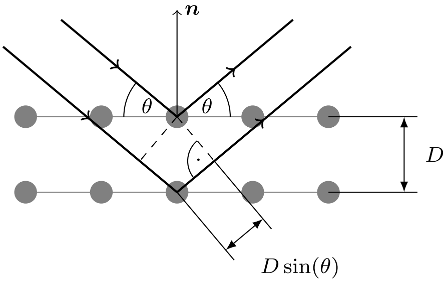

Fig. 1 Bragg diffraction; image based on Noyan and Cohen [27]

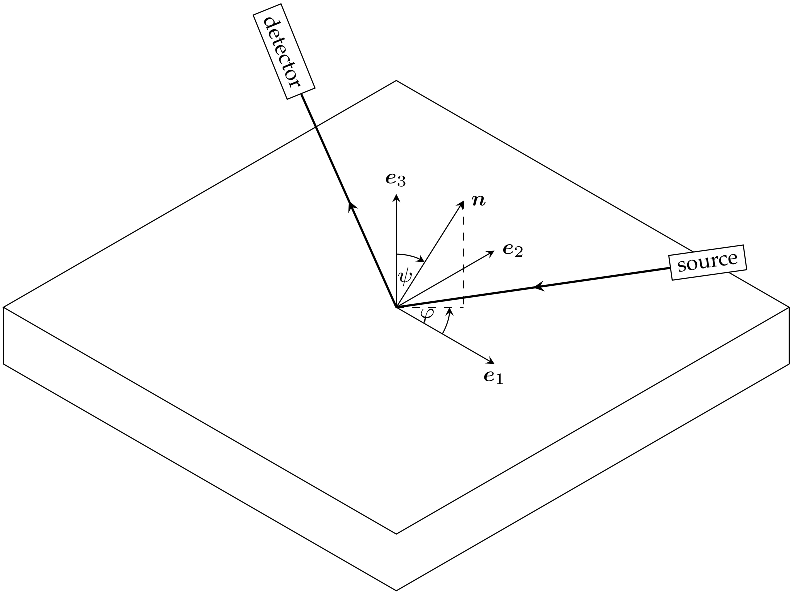

Fig. 2 Simplified geometry of the experimental setup for diffraction-based stress analysis

planes of type hkl, which in the cubic case is given by all permutations of hkl with any combination of signs. At this point, we impose no sample symmetry. Later derivations will be limited to the special case of texture-free polycrystals, which implies isotropic sample symmetry.

Figure 2 shows a simplified geometry of the experimental setup. A monochromatic X-ray originating from the source interacts with the sample at the origin point of the sample coordinate system $\boldsymbol{e}_i$. We assume the measurement volume of the diffraction experiment contains a sufficient amount of crystallites to ensure that diffracting lattice planes exist in approximately all spatial directions. Due to diffraction of the X-ray beam at the crystal lattice, diffraction cones form. Typically the diffracted signal can be recorded by cuts through the diffraction cones in specific orientations by means of appropriately positioned detectors. The unit normal vector $\boldsymbol{n}$ of the diffracting lattice plane family $\{hkl\}$ can be specified depending on the azimuth angle φ and the polar angle ψ by

$$\boldsymbol{n}(\varphi, \psi) = \cos(\varphi)\sin(\psi)\boldsymbol{e}_1 + \sin(\varphi)\sin(\psi)\boldsymbol{e}_2 + \cos(\psi)\boldsymbol{e}_3. \tag{4}$$

where $\boldsymbol{e}_i$ are the basis vectors of the fixed sample coordinate system.

In both Fig. 2 and Fig. 1, the vector $\boldsymbol{n}$ is the same. This correspondence defines the set g of crystal orientations for which diffraction can be experimentally observed under given angles,

$$g(\{hkl\}, \varphi, \psi) = \{\boldsymbol{Q} \in Orth^+ : \boldsymbol{n}(\{hkl\}, \boldsymbol{Q}) = \boldsymbol{n}(\varphi, \psi)\}. \tag{5}$$

In Fig. 1, diffraction is illustrated with a crystallite of one orientation. Regardless of any lattice symmetry, the set g includes all rotations of that orientation around $\boldsymbol{n}$. Therefore, g as a set is invariant with respect to arbitrary rotations around $\boldsymbol{n}$, i.e.,

$$g = \boldsymbol{R}(\boldsymbol{n}, \alpha) \star g = \{\boldsymbol{R}(\boldsymbol{n}, \alpha)\boldsymbol{Q} : \boldsymbol{Q} \in g\} \quad \forall \alpha \in [0, 2\pi]. \tag{6}$$

A direct calculation of g is possible by choosing one diffracting orientation $\boldsymbol{Q}_0$ and rotating around $\boldsymbol{n}$. A possible choice for $\boldsymbol{Q}_0$ can be calculated by first finding a rotation which maps the lattice normal vector in the reference configuration

$$\boldsymbol{n}((hkl), \mathbf{1}) = \frac{h\boldsymbol{e}_1 + k\boldsymbol{e}_2 + l\boldsymbol{e}_3}{\sqrt{h^2 + k^2 + l^2}} \tag{7}$$

to $\boldsymbol{e}_3$, and then multiplying with a rotation that maps $\boldsymbol{e}_3$ to the vector $\boldsymbol{n}(\varphi, \psi)$. $\boldsymbol{Q}_0$ can be written in Euler angles as

$$\varphi_1 = \varphi \tag{8}$$

$$\phi = \psi - \arccos(l) \tag{9}$$

$$\varphi_2 = \begin{cases} -\arcsin\left(\frac{k}{\sqrt{1-l^2)}}\right) & |l| \neq 1 \\ 0 & |l| = 1 \end{cases} \tag{10}$$

in the ZYZ convention, i.e., with intrinsic rotations around those three axes, as shown for φ and ψ in Fig. 2. Every permutation in $\{hkl\}$ yields a different $\boldsymbol{Q}_0$. The set g can then be written as

$$g(\{hkl\}, \varphi, \psi) = \{\boldsymbol{R}(\boldsymbol{n}, \alpha)\boldsymbol{Q}_0((hkl), \varphi, \psi) : \alpha \in [0, 2\pi), (hkl) \in \{hkl\}\}. \tag{11}$$

The use of the diffraction relation to analyze stresses is based on the lattice plane distance D implied by Equation (1). Residual stresses within the material cause elastic strains such that the stress-free lattice plane distance D_0 is compressed or elongated to the lattice plane distance D. As elastic strains are small in metals, small-deformation strains can be assumed. These are defined via

$$\boldsymbol{\varepsilon} = \mathrm{sym}(\mathrm{grad}\,(\boldsymbol{u})), \tag{12}$$

a kinematic assumption which entails that any changes of lattice orientation due to elastic deformations can be neglected. The lattice plane normal component of the strain is given by

$$\frac{D - D_0}{D_0} = \boldsymbol{\varepsilon} \cdot (\boldsymbol{n} \otimes \boldsymbol{n}). \tag{13}$$

The relationship between these purely elastic strains and the corresponding residual stresses is given by Hooke's Law

$$\boldsymbol{\sigma} = \mathbb{C}[\boldsymbol{\varepsilon}]. \tag{14}$$

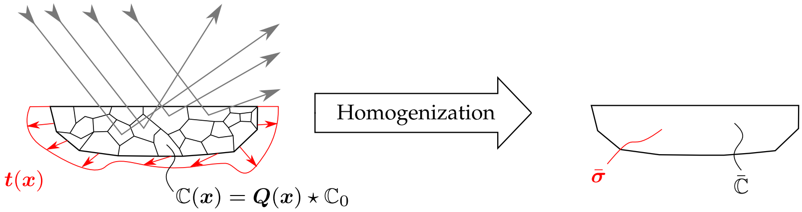

Fig. 3 Schematic of the irradiated crystallites versus a homogenized replacement problem

These stresses, strains and stiffnesses are in the following called local or microscale quantities. The local stiffness tensor $\mathbb{C}$ is specified by the cubic stiffness reference tensor $\mathbb{C}^{\mathrm{C}}$ of the crystallite aligned to $\boldsymbol{e}_i$, which is rotated by the local crystal orientation to yield

$$\mathbb{C} = \boldsymbol{Q} \star \mathbb{C}^{\mathrm{C}}. \tag{15}$$

In experimental applications, various assumptions made in the previous section do not hold exactly. For example, the beam is not perfectly monochromatic, but exhibits a wavelength distribution, and the crystallite does not have an ideal lattice, i.e., it contains lattice imperfections. As a result, measurements of the diffraction angle θ include statistical noise from various sources. When using the $\sin^2(\psi)$ technique, the statistically scattered θ values are integrated over to retrieve one single angle. Due to this averaging process, only $\langle D \rangle_g$, the statistical mean of the lattice plane distance over g, can be calculated from measurements. Taking this statistical mean over the stress-strain relationship leads to

$$\frac{\langle D \rangle_g - D_0}{D_0} = \langle \boldsymbol{\varepsilon} \rangle_g \cdot (\boldsymbol{n} \otimes \boldsymbol{n}) = (\boldsymbol{n} \otimes \boldsymbol{n}) \cdot \langle \mathbb{C}^{-1}[\boldsymbol{\sigma}] \rangle_g, \tag{16}$$

where $\boldsymbol{n}$ is unchanged by the averaging operation as it is constant for all $\boldsymbol{Q}$ in g as per the definition in Equation (5). Using this g-average, single-crystal lattice deformations are not available for analysis, yet the g-average is not a purely macroscopic polycrystal quantity, and as a partial average contains some information about local distributions.

Establishing a relation between $\langle \mathbb{C}^{-1}[\boldsymbol{\sigma}] \rangle_g$ and a macroscopically observable stress quantity requires various micromechanical assumptions. As depicted in Fig. 3, the beam irradiates multiple crystallites at once, generally many more than shown in this schematic drawing. At the edge of the irradiated material volume, generally, heterogeneous boundary conditions apply which depend on crystallites which are not irradiated. Problems of this kind are micromechanically simplified by defining a replacement problem with a homogeneous material $\bar{\mathbb{C}}$ and homogeneous loads as sketched in Fig. 3. The necessary condition for equivalence between the heterogeneous and homogeneous problems is the Hill-Mandel condition

$$\langle \boldsymbol{\sigma} \cdot \boldsymbol{\varepsilon} \rangle = \langle \boldsymbol{\sigma} \rangle \cdot \langle \boldsymbol{\varepsilon} \rangle \tag{17}$$

after Hill [11], which applies to divergence-free stress fields and kinematically compatible strain fields with homogeneous or periodic boundary conditions, regardless of whether the material behavior is linear or nonlinear. For irradiated crystallites embedded in a larger sample, neither homogeneous nor periodic boundary conditions cannot be assumed, but following an argument described by, among others, Kreher and Pompe [18, Sect. 2.5.2], the Hill-Mandel condition holds in the limit of an infinitely large sample, which in this case is given if an infinite number of very small grains is irradiated by the beam. In the X-ray diffraction setting, the Hill-Mandel condition is therefore an approximation that is improved as the number of grains under consideration increases. More accurate results are expected for finer-grained materials.

After applying the Hill-Mandel condition to the linear elastic strains and stresses in the polycrystal, the average strain energy density follows as

$$\bar{w} = \frac{1}{2}\langle \boldsymbol{\sigma} \cdot \boldsymbol{\varepsilon} \rangle = \frac{1}{2}\langle \boldsymbol{\sigma} \rangle \cdot \langle \boldsymbol{\varepsilon} \rangle, \tag{18}$$

and is therefore fully determined by the homogeneous effective stresses and strains

$$\bar{\boldsymbol{\sigma}} = \langle \boldsymbol{\sigma} \rangle, \quad \bar{\boldsymbol{\varepsilon}} = \langle \boldsymbol{\varepsilon} \rangle. \tag{19}$$

Thus, the material properties in the homogeneous replacement problem are fully described by the effective Hooke's Law

$$\bar{\boldsymbol{\sigma}} = \bar{\mathbb{C}}[\boldsymbol{\varepsilon}]. \tag{20}$$

In the absence of microscopically heterogeneous residual stresses such as those caused by a prior plastic deformation, the micromechanical problem is linear. Therefore, local strains are linear in effective stresses. Following Hill [11], this relationship is formalized by introducing the strain concentration tensor $\mathbb{A}$ defined by

$$\boldsymbol{\varepsilon}(\boldsymbol{x}) = \mathbb{A}(\boldsymbol{x})[\bar{\boldsymbol{\varepsilon}}]. \tag{21}$$

Exact knowledge of $\mathbb{A}(\boldsymbol{x})$ corresponds to full knowledge of the local stresses and strains. In the following, only the mean strain of all grains of a given orientation is needed, such that $\mathbb{A}$ can be understood as a function of $\boldsymbol{Q}$ instead of $\boldsymbol{x}$.

Averaging Hooke's Law on the microscale leads to

$$\bar{\boldsymbol{\sigma}} = \langle \mathbb{C}\mathbb{A} \rangle[\bar{\boldsymbol{\varepsilon}}], \tag{22}$$

thus leading to an explicit expression for the effective stiffness,

$$\bar{\mathbb{C}} = \langle \mathbb{C}\mathbb{A} \rangle, \tag{23}$$

which is major-symmetric as it can be calculated by differentiating Equation (18) by $\bar{\boldsymbol{\varepsilon}}$ twice.

Combining the concentration tensor with Equation (16) yields the fundamental XRD stress analysis equation

$$\begin{aligned} \frac{\langle D \rangle_g - D_0}{D_0} &= (\boldsymbol{n} \otimes \boldsymbol{n}) \cdot \langle \mathbb{A} \rangle_g [\bar{\boldsymbol{\varepsilon}}] \\ &= (\boldsymbol{n} \otimes \boldsymbol{n}) \cdot \langle \mathbb{A} \rangle_g \bar{\mathbb{C}}^{-1} [\bar{\boldsymbol{\sigma}}] \\ &= \bar{\mathbb{C}}^{-1} \langle \mathbb{A}^{\mathsf{TH}} \rangle_g [\boldsymbol{n} \otimes \boldsymbol{n}] \cdot \bar{\boldsymbol{\sigma}}. \end{aligned} \tag{24}$$

Following Behnken and Hauk [1], the second order tensor

$$\boldsymbol{F}(\varphi, \psi, \{hkl\}) = \bar{\mathbb{C}}^{-1} \langle \mathbb{A}^{\mathsf{TH}} \rangle_g [\boldsymbol{n} \otimes \boldsymbol{n}] \tag{25}$$

is called a stress factor. In the general form of Equation (24), the XRD equation is applicable to arbitrary crystal symmetries and textures. Its accuracy depends on finding an accurate estimate for the strain concentration $\mathbb{A}(\boldsymbol{Q})$.

2.2 Cubic Polycrystals Without Texture

2.2.1 Micromechanics of Polycrystals Without Texture

Before specifying $\mathbb{A}(\boldsymbol{Q})$, some micromechanical features of cubic polycrystals in particular can be applied to simplify Equation (24). If it can be assumed that the polycrystal exhibits neither crystallographic nor morphological texture, e.g., neither a preferred lattice orientation nor a preferred grain shape orientation, the material is statistically isotropic; see, e.g. Torquato [32]. All macroscopic quantities are then invariant under arbitrary rotations. In particular, the effective stiffness is required to have the form

$$\bar{\mathbb{C}} = 3\bar{K}\mathbb{P}^{\circ} + 2\bar{G}\mathbb{P}' \tag{26}$$

with the isotropic projectors $\mathbb{P}^{\circ}$ and $\mathbb{P}'$. Any quantity describing the single crystal which can be described via rotation from the reference orientation,

$$\mathbb{B} = \boldsymbol{Q} \star \mathbb{B}_0, \tag{27}$$

is in the statistical mean given by an isotropic projection. For a fourth-order tensor $\mathbb{B}$, since $\mathbb{P}^{\circ} \cdot \mathbb{P}^{\circ} = 1$ and $\mathbb{P}' \cdot \mathbb{P}' = 5$,

$$\begin{aligned} \langle \mathbb{B} \rangle &= \frac{\mathbb{P}^{\circ} \cdot \mathbb{B}_0}{\mathbb{P}^{\circ} \cdot \mathbb{P}^{\circ}} \, \mathbb{P}^{\circ} + \frac{\mathbb{P}' \cdot \mathbb{B}_0}{\mathbb{P}' \cdot \mathbb{P}'} \, \mathbb{P}', \\ &= (\mathbb{P}^{\circ} \cdot \mathbb{B}_0) \, \mathbb{P}^{\circ} + \frac{\mathbb{P}' \cdot \mathbb{B}_0}{5} \, \mathbb{P}'. \end{aligned} \tag{28}$$

For statistical isotropy, it is sufficient that there is neither a crystallographic nor a morphological texture in the overall statistics of the polycrystal. This does not necessarily imply that the grain shape is statistically independent of the grain orientation. When considering the interaction of grains of a single specific orientation with their surroundings, assuming that grain shapes and grain textures are uncorrelated leads to a morphological isotropy of the geometrical interface between the statistically average grain and its surroundings. This abstract notion of symmetry of phasewise statistical properties of microstructures is foundational to various micromechanical methods, e.g. the Hashin-Shtrikman approach as discussed by Willis [37]. In the case of a crystallite with anisotropic material properties in a morphologically and orientation-wise uncorrelated isotropic polycrystal, the morphology and the orientation of neighbouring grains are statistically isotropic and do not contribute to any anisotropy, meaning that the single-grain interaction problem is statistically of the same symmetry as the grain. In particular, the strain concentration tensor $\mathbb{A}(\boldsymbol{Q})$ averaged over all grains of a single orientation $\boldsymbol{Q}$ is given by

$$\mathbb{A}(\boldsymbol{Q}) = \boldsymbol{Q} \star \mathbb{A}_0. \tag{29}$$

Due to the symmetry assumption for the grain shape and surroundings, the fourth-order tensor $\mathbb{A}$ has the same symmetry as the lattice. For example, for a cubic material, $\mathbb{A}$ is a cubic tensor with symmetry axes $\boldsymbol{g}_i = \boldsymbol{Q}\boldsymbol{e}_i$. Given the irregular grain shapes encountered in practice, the symmetry assumption above might seem insufficiently motivated. However, the analytical approximations most often employed in the calculation of isotropic stress factors generally rely on stronger assumptions from which Equation (29) follows regardless.

In the special case of cubic local symmetry, further results can be derived. Based on the eigentensor decomposition described by, among others, Kocks et al. [14], a cubic fourth order tensor in the reference orientation admits the projector decomposition

$$\mathbb{B}_0 = \lambda_1^{\mathrm{B}}\mathbb{P}_1^{\mathrm{C}} + \lambda_2^{\mathrm{B}}\mathbb{P}_2^{\mathrm{C}} + \lambda_3^{\mathrm{B}}\mathbb{P}_3^{\mathrm{C}}, \tag{30}$$

with the cubic projectors

$$\mathbb{P}_1^{\mathrm{C}} = \mathbb{P}^{\circ}, \tag{31}$$

$$\mathbb{P}_2^{\mathrm{C}} = \mathbb{D} - \mathbb{P}^{\circ}, \tag{32}$$

$$\mathbb{P}_3^{\mathrm{C}} = \mathbb{I}^{\mathrm{S}} - \mathbb{D}. \tag{33}$$

The fourth-order cubic tensor $\mathbb{D}$ is a constant describing the reference orientation which reads

$$\mathbb{D} = \sum_{i=1}^{3} \boldsymbol{e}_i \otimes \boldsymbol{e}_i \otimes \boldsymbol{e}_i \otimes \boldsymbol{e}_i. \tag{34}$$

Because $\mathbb{P}_1^{\mathrm{C}}$ is the isotropic spherical projector while $\mathbb{P}_2^{\mathrm{C}}$ and $\mathbb{P}_3^{\mathrm{C}}$ map spherical tensors to zero, the spherical and deviatoric modes of stress and strain are entirely decoupled in a cubic polycrystal. Furthermore, because $\mathbb{P}_1^{\mathrm{C}}$ is isotropic and therefore independent of the grain orientation, the cubic stresses and strains are homogeneous. The effective compression modulus is therefore explicitly given using the first eigenvalue of the stiffness $\mathbb{C}$,

$$3\bar{K} = \lambda_1^{\mathrm{C}}. \tag{35}$$

With the spherical homogenization problem solved, only the deviatoric parts of the strain concentration tensor must be specified. For a cubic polycrystal with no texture and no correlation between grain orientation and grain shape, the effective shear modulus is fully sufficient to specify $\mathbb{A}(\boldsymbol{Q})$. This parametrization of the micromechanical problem is particularly useful because $\bar{G}$ is a macroscopically observable parameter that can be measured using a simple tensile test. A derivation including explicit formulas is detailed in Appendix A.

2.2.2 Simplified XRD Problem

Following Behnken and Hauk [1], the stress factor for a statistically isotropic polycrystal is

$$\boldsymbol{F}(\varphi, \psi, hkl) = s_1(hkl)\boldsymbol{I} + \frac{1}{2}s_2(hkl)\boldsymbol{n}(\varphi, \psi) \otimes \boldsymbol{n}(\varphi, \psi), \tag{36}$$

where s_1 and $½s_2$ are called diffraction elastic constants (DECs).

Comparison with the explicit formula given in Appendix B for cubic crystals with spherical mean grains yields

$$s_1 = \frac{-5\lambda_1^{\mathrm{C}}\left(2\Gamma\lambda_2^{\mathrm{C}} + 3\Gamma\lambda_3^{\mathrm{C}} - 10\Gamma\bar{G} - \lambda_3^{\mathrm{C}} + 2\bar{G}\right) + 4\bar{G}\left(\lambda_2^{\mathrm{C}} - \lambda_3^{\mathrm{C}}\right)}{12\lambda_1^{\mathrm{C}}\bar{G}\left(\lambda_2^{\mathrm{C}} - \lambda_3^{\mathrm{C}}\right)}, \tag{37}$$

$$\frac{s_2}{2} = \frac{5\left(2\Gamma\lambda_2^{\mathrm{C}} + 3\Gamma\lambda_3^{\mathrm{C}} - 10\Gamma\bar{G} - \lambda_3^{\mathrm{C}} + 2\bar{G}\right)}{4\bar{G}\left(\lambda_2^{\mathrm{C}} - \lambda_3^{\mathrm{C}}\right)}. \tag{38}$$

The lattice plane parameter 3Γ describes the influence of the lattice plane and is defined as

$$3\Gamma = 3\frac{h^2k^2 + h^2l^2 + k^2l^2}{\left(h^2 + k^2 + l^2\right)^2}. \tag{39}$$

Depending on the experimental conditions, pure plane stress conditions can sometimes be assumed in $\sin^2(\psi)$ analysis, particularly if the effective penetration depth of the X-rays is in the range of a few micrometers. In that case, Equation (24) takes the form

$$\langle \boldsymbol{\varepsilon} \rangle_g \cdot (\boldsymbol{n} \otimes \boldsymbol{n}) = \frac{s_2}{2}(\bar{\sigma}_{11}\cos^2(\varphi) + \bar{\sigma}_{12}\sin(2\varphi) + \bar{\sigma}_{22}\sin^2(\varphi))\sin^2(\psi) + s_1(\bar{\sigma}_{11} + \bar{\sigma}_{22}), \tag{40}$$

such that $\langle \boldsymbol{\varepsilon} \rangle_g$ is linear with respect to $\sin^2(\psi)$. This linearity may be lost if any of the above assumptions are violated, e.g. if stress gradients, texture, or shear stresses $\bar{\sigma}_{13}$ or $\bar{\sigma}_{23}$ are present; cf. Noyan and Cohen [27].

3 Singular Approximation Methods

3.1 General Singular Approximation for Polycrystals Without Texture

This section discusses the Voigt, Reuss, Hashin-Shtrikman and self-consistent (also known as Eshelby-Kröner) models of local strain fields in a polycrystal. All of these approximation methods can be characterized as special cases of the singular approximation due to Fokin [7].

The singular approximation formally assumes that the non-singular part of Green's tensor is negligible, as described for the case of a cubic polycrystal by Böhlke et al. [2]. In practice, this results in the same approximations for local strains as the Hashin-Shtrikman formalism as described by Willis [38] and others. In particular, the strain concentration tensor is given as

$$\mathbb{A} = \mathbb{L}\langle\mathbb{L}\rangle^{-1} \tag{41}$$

with

$$\mathbb{L} = (\mathbb{C} - \mathbb{C}_{\mathrm{r}} + \mathbb{P}_{\mathrm{r}}^{-1})^{-1}. \tag{42}$$

The reference stiffness $\mathbb{C}_{\mathrm{r}}$ is in general left-, right- and major-symmetric as well as positive-definite. A microstructural interpretation of $\mathbb{C}_{\mathrm{r}}$ is possible via the ellipsoidal inclusion problem solved by Eshelby [5], but in the context of this work it is sufficient to consider $\mathbb{C}_{\mathrm{r}}$ as a parameter of the singular approximation. $\mathbb{P}_{\mathrm{r}}$ depends on $\mathbb{C}_{\mathrm{r}}$, but also reflects the morphology of the material. In the case of a statistically isotropic polycrystal with a grain shape which is spherical in the mean, $\mathbb{C}_{\mathrm{r}}$ is isotropic and $\mathbb{P}_{\mathrm{r}}$ is given by Willis [38] as

$$\mathbb{P}_{\mathrm{r}} = \frac{1}{3K_{\mathrm{r}} + 4G_{\mathrm{r}}}\mathbb{P}^{\circ} + \frac{3(K_{\mathrm{r}} + 2G_{\mathrm{r}})}{5G_{\mathrm{r}}(3K_{\mathrm{r}} + 4G_{\mathrm{r}})}\mathbb{P}'. \tag{43}$$

For cubic polycrystals, the assumption of a cubic strain concentration tensor in Equation (29) is fulfilled for an isotropic $\mathbb{C}_{\mathrm{r}}$, since

$$\mathbb{A} = \boldsymbol{Q} \star \left((\mathbb{C}_0 - \mathbb{C}_{\mathrm{r}} + \mathbb{P}_{\mathrm{r}}^{-1})^{-1}\langle\mathbb{L}\rangle^{-1}\right) = \boldsymbol{Q} \star \mathbb{A}_0. \tag{44}$$

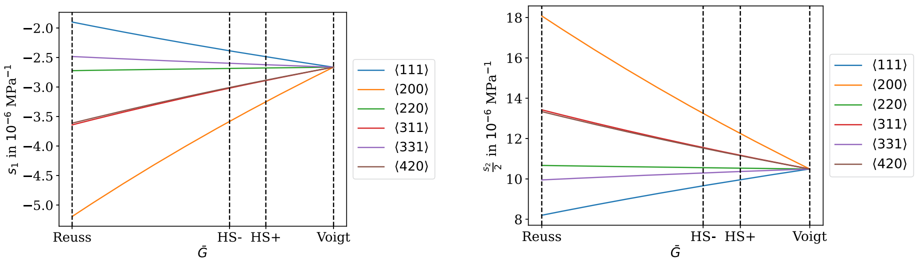

(a) s_1 depending on $\bar{G}$ for fcc planes

(b) ½s_2 depending on $\bar{G}$ for fcc planes

Fig. 4 DECs for statistically isotropic copper

The effective singular approximation stiffness is given for the general anisotropic case by Walpole [34] in the form

$$\bar{\mathbb{C}}^{\mathrm{SA}} = \langle \mathbb{L} \rangle^{-1} + \mathbb{C}_{\mathrm{r}} - \mathbb{P}_{\mathrm{r}}^{-1}. \tag{45}$$

With the symmetries detailed above, the shear modulus can be represented by

$$\bar{G}^{\mathrm{SA}} = \frac{16G_{\mathrm{r}}^2\lambda_2^{\mathrm{C}} + 24G_{\mathrm{r}}^2\lambda_3^{\mathrm{C}} + 18G_{\mathrm{r}}K_{\mathrm{r}}\lambda_2^{\mathrm{C}} + 27G_{\mathrm{r}}K_{\mathrm{r}}\lambda_3^{\mathrm{C}} + 30G_{\mathrm{r}}\lambda_2^{\mathrm{C}}\lambda_3^{\mathrm{C}} + 15K_{\mathrm{r}}\lambda_2^{\mathrm{C}}\lambda_3^{\mathrm{C}}}{2\left(40G_{\mathrm{r}}^2 + 45G_{\mathrm{r}}K_{\mathrm{r}} + 18G_{\mathrm{r}}\lambda_2^{\mathrm{C}} + 12G_{\mathrm{r}}\lambda_3^{\mathrm{C}} + 9K_{\mathrm{r}}\lambda_2^{\mathrm{C}} + 6K_{\mathrm{r}}\lambda_3^{\mathrm{C}}\right)}. \tag{46}$$

For the sake of brevity, we do not re-derive the DECs by using the explicitly given strain concentration tensor of Equation (44). Instead, with the strain concentration tensor fulfilling Equation (29), Equation (46) can be used together with Equation (37) and Equation (38) to calculate DECs. Theoretically, as the choice of G_{r} and K_{r} uniquely specifies $\bar{G}$, either parametrization yields the same result. If $\bar{G}$ is already known, e.g. from experimental measurements, using the singular approximation framework is not necessary. We introduce the singular approximation because various possible choices of G_{r} and K_{r} can be motivated on theoretical grounds to yield established micromechanical models, and because the singular approximation is amenable to a possible future generalization for textured polycrystals, unlike the direct method using $\bar{G}$.

As an example, we consider statistically isotropic pure copper with single crystal elastic constants

$$C_{1111} = 170.2 \text{ GPa}, \qquad C_{1122} = 114.9 \text{ GPa}, \qquad C_{1212} = 61.0 \text{ GPa}, \tag{47}$$

taken from Simmons and Wang [30]. The microstructure is not specified, leading to an unknown effective shear stiffness. The resulting DECs are depicted in Fig. 4. This diagram shows a monotonic relationship between the effective shear stiffness and the DECs which depends on the considered lattice plane. The range of effective shear moduli spans all values that can be realized by the singular approximation if $\mathbb{C}_{\mathrm{r}}$ is positive semidefinite and isotropic. The specific micromechanical models indicated by dashed lines are explained in the following.

3.2 Specific Models

3.2.1 Voigt and Reuss Bounds

The Voigt ($\mathbb{C}_+$) and Reuss ($\mathbb{C}_-$) estimates of the effective stiffness are motivated by the direct assumption of constant strains and constant stresses in their original formulations by Voigt [33] and Reuss [28], respectively. These assumptions are written in terms of strain concentration tensors as

$$\mathbb{A}^+ = \mathbb{I}^{\mathrm{S}}, \tag{48}$$

$$\mathbb{A}^- = \mathbb{C}^{-1}\mathbb{C}_-. \tag{49}$$

By using the singular approximation, Voigt and Reuss estimates can instead be recovered as limits implied by the positive definiteness of $\mathbb{C}_{\mathrm{r}}$,

$$\mathbb{C}_+ = \lim_{\mathbb{C}_{\mathrm{r}}^{-1}\to 0} \bar{\mathbb{C}}^{\mathrm{SA}} = \langle \mathbb{C} \rangle, \tag{50}$$

$$\mathbb{C}_- = \lim_{\mathbb{C}_{\mathrm{r}}\to 0} \bar{\mathbb{C}}^{\mathrm{SA}} = \langle \mathbb{C}^{-1} \rangle^{-1}. \tag{51}$$

The isotropic DECs for the Voigt estimate are

$$s_1^+ = \frac{1}{3\lambda_1^{\mathrm{C}}} - \frac{5}{3(2\lambda_2^{\mathrm{C}} + 3\lambda_3^{\mathrm{C}})}, \tag{52}$$

$$\frac{s_2^+}{2} = \frac{5}{2\lambda_2^{\mathrm{C}} + 3\lambda_3^{\mathrm{C}}}. \tag{53}$$

For the Reuss estimate,

$$s_1^- = \left(\Gamma - \frac{1}{3}\right)\left(\frac{1}{\lambda_3^{\mathrm{C}}} - \frac{1}{\lambda_2^{\mathrm{C}}}\right), \tag{54}$$

$$\frac{s_2{}^-}{2} = \frac{3\Gamma}{\lambda_3^{\mathrm{C}}} - \frac{1}{\lambda_2^{\mathrm{C}}}\left(3\Gamma - 1\right). \tag{55}$$

The Voigt and Reuss estimates represent strict bounds for the effective strain energy density. As a consequence, for all possible microstructures, the effective stiffnesses are bounded by

$$\mathbb{C}_+ \geq \bar{\mathbb{C}} \geq \mathbb{C}_- \tag{56}$$

in the sense that $\mathbb{C}_+ - \bar{\mathbb{C}}$ is required to be positive semidefinite. Similarly, the corresponding Voigt and Reuss DECs form bounds on the possible values of the DECs, as shall be discussed in the following. In the specific case of statistically isotropic cubic polycrystals, the bounds on the effective shear modulus are

$$G_+ \geq \bar{G} \geq G_-. \tag{57}$$

Because both $s_1(\bar{G})$ and $\frac{1}{2}s_2(\bar{G})$ are monotonic in $\bar{G}$, these bounds then also hold for s_1 and $\frac{1}{2}s_2$. Any experimentally measured values of the DECs which violate these bounds contradict underlying micromechanical assumptions. The Voigt and Reuss estimates are first-order bounds depending only on the crystallographic texture and the material properties, meaning that they hold for arbitrarily asymmetric grain shapes. If they are clearly violated beyond measurement error, possible explanations include material imperfections of the polycrystal such as pores or material inhomogeneities.

The Reuss DECs depend on 3Γ and match the values of the Voigt elastic constants at

$$3\Gamma = \frac{3\lambda_3^{\mathrm{C}}}{2\lambda_2^{\mathrm{C}} + 3\lambda_3^{\mathrm{C}}}, \tag{58}$$

such that for higher 3Γ, the upper and lower bounds swap places. Because Voigt and Reuss values are strict bounds, all methods for calculating DECs, including experimental results, are required to coincide at this specific value of 3Γ.

3.2.2 Hashin-Shtrikman Bounds

Tighter bounds on the effective stiffness can be recovered using additional assumptions. According to Willis [37], the assumption that the two-point statistic of the grain orientation distribution has ellipsoidal symmetry is sufficient to prove that for the Hashin-Shtrikman (HS) bounds,

$$\mathbb{C}_{\mathrm{HS}+} \geq \bar{\mathbb{C}} \geq \mathbb{C}_{\mathrm{HS}-} \tag{59}$$

holds in the sense of positive semidefiniteness. The upper HS bound is recovered from the singular approximation by choosing

$$\mathbb{C}_{\mathrm{r}} \geq \mathbb{C}_0 \tag{60}$$

for an isotropic $\mathbb{C}_{\mathrm{r}}$ that is as small as possible, where $\mathbb{C}_0$ is the upper zeroth-order bound of Nadeau and Ferrari [26]. Specifically for cubic crystals, the tightest upper bound is recovered by choosing an isotropic $\mathbb{C}_{\mathrm{r}}$ with

$$3K_{\mathrm{r}} = \lambda_1^{\mathrm{C}}, \tag{61}$$

$$2G_{\mathrm{r}} = \max(\lambda_2^{\mathrm{C}}, \lambda_3^{\mathrm{C}}). \tag{62}$$

Following Lobos and Böhlke [23], the lower HS bounds are recovered by similarly choosing

$$\mathbb{C}_{\mathrm{r}}^{-1} \geq \mathbb{C}_0^{-1}, \tag{63}$$

which leads to

$$3K_{\mathrm{r}} = \lambda_1^{\mathrm{C}}, \tag{64}$$

$$2G_{\mathrm{r}} = \min(\lambda_2^{\mathrm{C}}, \lambda_3^{\mathrm{C}}). \tag{65}$$

The formula for the lower HS bound with $\lambda_2^{\mathrm{C}} < \lambda_3^{\mathrm{C}}$ corresponds to the upper HS bound with $\lambda_2^{\mathrm{C}} > \lambda_3^{\mathrm{C}}$. Either case results in the effective shear modulus

$$\bar{G}^{\mathrm{HS}}(G_{\mathrm{r}} = \lambda_2^{\mathrm{C}}) = \frac{\lambda_2^{\mathrm{C}}\left(3\lambda_1^{\mathrm{C}}\lambda_2^{\mathrm{C}} + 7\lambda_1^{\mathrm{C}}\lambda_3^{\mathrm{C}} + 8(\lambda_2^{\mathrm{C}})^2 + 27\lambda_2^{\mathrm{C}}\lambda_3^{\mathrm{C}}\right)}{2\left(9\lambda_1^{\mathrm{C}}\lambda_2^{\mathrm{C}} + \lambda_1^{\mathrm{C}}\lambda_3^{\mathrm{C}} + 29(\lambda_2^{\mathrm{C}})^2 + 6\lambda_2^{\mathrm{C}}\lambda_3^{\mathrm{C}}\right)}. \tag{66}$$

The corresponding other bound reads

$$\bar{G}^{\mathrm{HS}}(G_{\mathrm{r}} = \lambda_3^{\mathrm{C}}) = \frac{\lambda_3^{\mathrm{C}} \left(11\lambda_1^{\mathrm{C}}\lambda_2^{\mathrm{C}} + 9\lambda_1^{\mathrm{C}}\lambda_3^{\mathrm{C}} + 46\lambda_2^{\mathrm{C}}\lambda_3^{\mathrm{C}} + 24(\lambda_3^{\mathrm{C}})^2\right)}{2\left(3\lambda_1^{\mathrm{C}}\lambda_2^{\mathrm{C}} + 17\lambda_1^{\mathrm{C}}\lambda_3^{\mathrm{C}} + 18\lambda_2^{\mathrm{C}}\lambda_3^{\mathrm{C}} + 52(\lambda_3^{\mathrm{C}})^2\right)}. \tag{67}$$

DECs can be recovered using Equation (37) and Equation (38).

Similarly to the Voigt-Reuss bounds, if the HS shear modulus bounds the effective shear modulus, the HS DECs are bounds on DECs as well. The underlying assumption that the two-point statistic of the grain orientation distribution has spherical symmetry is a statistical assumption that can be fulfilled even when any given grain has a non-spherical shape.

3.2.3 Self-Consistent (Eshelby-Kröner) Approximation

The self-consistent approximation (sometimes called the Eshelby-Kröner approximation in materials science after Eshelby [5] and Kröner [19]) is recovered from the singular approximation by setting $\mathbb{C}_{\mathrm{r}} = \bar{\mathbb{C}}$. With $\bar{\mathbb{C}}$ itself depending on $\mathbb{C}_{\mathrm{r}}$ according to Equation (45), a non-linear equation results. In the general anisotropic case, this equation is solved numerically at some expense, cf. Behnken and Hauk [1]. For statistically isotropic cubic polycrystals, the compression modulus is

$$K_{\mathrm{r}} = \bar{K} = \lambda_1^{\mathrm{C}}. \tag{68}$$

With $\bar{G}$ from Equation (46), the self-consistent approach results in the cubic equation

$$16\bar{G}^3 + \left(18\lambda_1^{\mathrm{C}} + 4\lambda_2^{\mathrm{C}}\right)\bar{G}^2 + \left(-3\lambda_1^{\mathrm{C}}\lambda_3^{\mathrm{C}} - 6\lambda_2^{\mathrm{C}}\lambda_3^{\mathrm{C}}\right)\bar{G} - 3\lambda_1^{\mathrm{C}}\lambda_2^{\mathrm{C}}\lambda_3^{\mathrm{C}} = 0 \tag{69}$$

noted by Willis [38] among others. According to Descartes' rule of signs, this equation has exactly one positive solution. From that $\bar{G}$, DECs can be calculated via Equation (37) and Equation (38).

Again, a mean spherical grain shape has been assumed for this calculation. In cases with significant morphological texture, i.e., rolled sheet metal, a mean ellipsoidal grain shape can be incorporated into the self-consistent approximation via a different choice of $\mathbb{P}_{\mathrm{r}}$, which significantly complicates the calculations.

4 Maximum Entropy Method

4.1 MEM for Uniform Textured Polycrystals

The micromechanical Maximum Entropy Method as first described by Kreher and Pompe [17] applies the method of entropy maximization pioneered by Jaynes [13] in statistical thermodynamics to micromechanics of random heterogeneous continua. By maximizing Shannon's information entropy of the probability distribution of stresses and strains, an estimate of that probability distribution is derived. Unlike classical homogenization approaches, the MEM approach is not based on directly solving the quasi-static local balance of linear momentum. The continuum-mechanical conditions that the stress field is divergence-free and the strain field kinematically compatible are instead incorporated into entropy maximization by prescribing the Hill-Mandel condition, which follows from those conditions, as a constraint to the optimization. Additionally, the effective loading and the effective material properties are incorporated by prescribing the effective stress and strain values as constraints. Unlike the singular approximation methods described above, no local symmetry condition or average grain shape is assumed a priori. The MEM has been found in a numerical study by Gehrig et al. [9] to yield precise estimates for stress statistics of elastic polycrystals in particular.

A short summary of the derivation of the MEM formulas is given in Appendix C. The interested reader is referred to Krause and Böhlke [15] for a more complete introduction. For single-phase textured polycrystals of arbitrary symmetry, the MEM approximation for local strains results to

$$p_1(\boldsymbol{\varepsilon}, \boldsymbol{Q}) = \frac{f(\boldsymbol{Q})}{\sqrt{(2\pi)^6 \det(\mathbb{K})}} \exp\left(-\frac{1}{2}(\boldsymbol{\varepsilon}-\boldsymbol{\gamma}) \cdot \mathbb{K}^{-1}[\boldsymbol{\varepsilon}-\boldsymbol{\gamma}]\right), \tag{70}$$

$$\mathbb{K} = k\boldsymbol{Q} \star \mathbb{C}_0^{-1}, \tag{71}$$

$$\boldsymbol{\gamma} = (\boldsymbol{Q} \star \mathbb{C}_0^{-1})[\boldsymbol{\mu}_\varepsilon] + \boldsymbol{\mu}_\sigma, \tag{72}$$

$$\boldsymbol{\mu}_\varepsilon = \mathbb{C}_-(\mathbb{C}_+ - \mathbb{C}_-)^+(\mathbb{C}_+ - \bar{\mathbb{C}})[\bar{\boldsymbol{\varepsilon}}], \tag{73}$$

$$\boldsymbol{\mu}_\sigma = \bar{\boldsymbol{\varepsilon}} - (\mathbb{C}_+ - \mathbb{C}_-)^+(\mathbb{C}_+ - \bar{\mathbb{C}})[\bar{\boldsymbol{\varepsilon}}], \tag{74}$$

$$k = \frac{1}{6}\bar{\boldsymbol{\varepsilon}} \cdot (\mathbb{C}_+ - \bar{\mathbb{C}})(\mathbb{C}_+ - \mathbb{C}_-)^+(\bar{\mathbb{C}} - \mathbb{C}_-)[\bar{\boldsymbol{\varepsilon}}]. \tag{75}$$

$\mathbb{C}_+$ and $\mathbb{C}_-$ are the Voigt and Reuss bounds as given in Equation (50) and Equation (51), respectively. For any fourth-order tensor $\mathbb{B}$, $\mathbb{B}^+$ denotes the Moore-Penrose pseudoinverse, which can be calculated by using any normalized matrix representation of $\mathbb{B}$ such as the Kelvin-Mandel or harmonic representation as described by Krause and Böhlke [16].

The strain concentration tensor implied by the MEM for textured polycrystals depends on the anisotropic effective stiffness tensor $\bar{\mathbb{C}}$ and the single crystal orientation $\boldsymbol{Q}$ as

$$\mathbb{A}(\boldsymbol{Q}) = \left((\boldsymbol{Q} \star \mathbb{C}_0^{-1})\mathbb{C}_- - \mathbb{I}^{\mathrm{S}}\right)(\mathbb{C}_+ - \mathbb{C}_-)^+(\mathbb{C}_+ - \bar{\mathbb{C}}) + \mathbb{I}^{\mathrm{S}}. \tag{76}$$

Note that for $\bar{\mathbb{C}} \to \mathbb{C}_+$ and $\bar{\mathbb{C}} \to \mathbb{C}_-$, the strain concentration tensors for the Voigt and Reuss estimates given in Sect. 3.2.1 result.

4.2 Application of the MEM to XRD Stress Analysis

In the following, an isotropic uniform polycrystal with cubic stiffness eigenvalues λ_1^C, λ_2^C, λ_3^C is assumed. As discussed in Sect. 3.2.1,

$$\mathbb{C}_+ = \lambda_1^C \mathbb{P}_1 + \left(\frac{2}{5}\lambda_2^C + \frac{3}{5}\lambda_3^C\right)\mathbb{P}_2 = \lambda_1^C \mathbb{P}_1 + 2G_+\mathbb{P}_2,$$

$$\mathbb{C}_- = \lambda_1^C \mathbb{P}_1 + \frac{5\lambda_2^C\lambda_3^C}{2\lambda_3^C + 3\lambda_2^C}\mathbb{P}_2 = \lambda_1^C \mathbb{P}_1 + 2G_-\mathbb{P}_2,$$

$$\bar{\mathbb{C}} = \lambda_1^C \mathbb{P}_1 + 2\bar{G}\mathbb{P}_2.$$

Because the compression modulus is homogeneous, the Moore-Penrose pseudoinverse degenerates to an inversion on the space of deviatoric second order tensors, and Equations (72)–(75) simplify to

$$\boldsymbol{\mu}_\varepsilon = \frac{2G_-(G_+ - \bar{G})}{G_+ - G_-}\mathrm{dev}(\bar{\boldsymbol{\varepsilon}}), \tag{77}$$

$$\boldsymbol{\mu}_\sigma = \bar{\boldsymbol{\varepsilon}} - \frac{G_+ - \bar{G}}{G_+ - G_-}\operatorname{dev}(\bar{\boldsymbol{\varepsilon}}), \tag{78}$$

$$k = \frac{1}{6}\|\operatorname{dev}(\bar{\boldsymbol{\varepsilon}})\|^2 \frac{\left(G_+ - \bar{G}\right)\left(\bar{G} - G_-\right)}{G_+ - G_-}. \tag{79}$$

As a consequence, Equation (76) simplifies to

$$\mathbb{A}(\boldsymbol{Q}) = \boldsymbol{Q} \star \mathbb{A}_0, \tag{80}$$

$$\mathbb{A}_0 = \mathbb{I}^{\mathrm{S}} + \frac{G_+ - \bar{G}}{G_+ - G_-}\sum_{\alpha=2}^{3}\frac{2G_- - \lambda_\alpha^{\mathrm{C}}}{\lambda_\alpha^{\mathrm{C}}}\mathbb{P}_\alpha^{\mathrm{C}}. \tag{81}$$

Because $\mathbb{A}$ has cubic symmetry, the formulas derived in Sect. 2.2.1 apply. In fact, the formulas derived in Appendix A yield the exact same result as the MEM. The reason for this is that the results in Appendix A are based on assuming the Hill-Mandel condition, which is also an optimization constraint for the MEM. However, for deriving the classical micromechanical formulas, we also assumed non-correlatedness between morphological and crystallographic textures. It appears that when assuming maximal entropy of the joint probability distribution of strains and material properties, this non-correlatedness follows in some indirect manner, at least in the present case of texture-free polycrystals.

4.3 Influence of Elastic Heterogeneity on Diffraction Measurements

In polycrystalline microstructures, the interaction of differently-oriented grains leads to heterogeneous stress and strain fields even if eigenstrains are not considered. As shown by Gehrig et al. [9], the strain covariances given by the MEM are an accurate approximation for cubic polycrystals. Using Equation (71), the component of the covariance in the lattice plane normal direction is given by

$$K_n = \mathbb{K} \cdot \boldsymbol{n}(\varphi, \psi)^{\otimes 4} \tag{82}$$

$$= k\left(\frac{2}{3\lambda_2^{\mathrm{C}}}(1 - 3\Gamma) + \frac{1}{\lambda_3^{\mathrm{C}}}\Gamma\right). \tag{83}$$

As an example, for pure copper with single crystal elastic constants as given in Equation (47), K_n is maximal for $3\Gamma = 0$. In that case, the standard deviation of the lattice plane normal strain is

$$\sqrt{K_n^{\mathrm{Cu}}(3\Gamma = 0)} \approx 0.080\|\operatorname{dev}(\bar{\boldsymbol{\varepsilon}})\|. \tag{84}$$

Assuming that there are no other sources of fluctuations in the lattice normal distance D, its deviation results as

$$\sqrt{\langle D^2\rangle - \langle D\rangle^2} = 0.080\|\operatorname{dev}(\bar{\boldsymbol{\varepsilon}})\| D_0. \tag{85}$$

Since $\bar{\boldsymbol{\varepsilon}}$ is generally on the order of 10^{-4}, the effect of the elastic heterogeneity is negligible compared to other sources of measurement fluctuations in experimental practice.

5 Full-Field XRD Simulations

5.1 Full-Field Simulation Method

To validate the theoretical result, full-field microstructure simulations with solvers based on the fast Fourier transform (FFT) according to the approach introduced by Moulinec and Suquet [25] are used. The conjugate gradient method proposed by Zeman et al. [39] is chosen as an optimization algorithm. Ringing artifacts, also called Gibbs' oscillations, are minimized by relying upon the staggered grid discretization [29]. All calculations were carried out using the FFTW library for Python 3 [8]. Further details on the FFT-based solver used can be found in Wicht et al. [35] and Wicht et al. [36].

Statistically isotropic microstructures of varying size distributions are computationally generated. To this end, the algorithms described by Kuhn et al. [20] are used. The resulting microstructures are Laguerre tesselations with grain orientations which realize a prescribed texture state with particular accuracy. As is usual for FFT-based calculations, the microstructures are discretized using cubic elements of equal size, in the following called voxels.

There are three sources of numerical error which will be considered separately in the following. The first is discretization error, which depends on the fineness of the resolution, i.e., the number of voxels used for the microstructure. The second is representativeness error, which is present if the artificially generated microstructure is not representative of the theoretical infinite microstructure underlying it, such as the generated microstructure not being perfectly statistically isotropic. The third is the solver error, which is the precision to which the Lippman-Schwinger equation is numerically solved. This value can be set to be smaller than the other errors by orders of magnitude and will not be considered.

The FFT-based solver used requires periodic boundary conditions. Therefore, any simulations approximate the behaviour of bulk material, not surface material. While, in the following section, an effective plane stress $\bar{\boldsymbol{\sigma}}$ is prescribed, the local stresses $\boldsymbol{\sigma}$ are not planar in every material point, as they would be at a free surface. The theoretical models used to compute DECs share the same limitation. As these models are well-established, we assume in the following that the difference between plane-stress bulk behaviour and surface behaviour can be neglected in practice.

5.2 XRD Simulation

Full-field simulations provide the entire local strain fields, from which $\boldsymbol{\varepsilon} \cdot (\boldsymbol{n} \otimes \boldsymbol{n})$ can be calculated directly. DECs can then be calculated by linear regression on simulated D-vs-$\sin^2(\psi)$ curves. The main difficulty of the process lies in the evaluation of averages over the set g, because only a finite number of discrete grain orientations are present, such that for almost all angles, there are no grains exactly fulfilling the underlying condition in Equation (5)

$$\boldsymbol{n}(\varphi, \psi) = \boldsymbol{n}(\{hkl\}, \boldsymbol{Q}). \tag{86}$$

In experimental practice, this condition can be violated because small misalignments do not prohibit diffraction. A full physical consideration of the underlying effects is difficult. We calculate diffraction misalignment as the distance between $\boldsymbol{Q}$ and $g(\{hkl\}, \varphi, \psi)$,

$$d = \min_{\alpha} \min_{(hkl)\in\{hkl\}} \|\boldsymbol{R}(\boldsymbol{n}, \alpha)\, \boldsymbol{Q}_0((hkl), \varphi, \psi) - \boldsymbol{Q}\|, \tag{87}$$

where the SO(3) distance by Larochelle et al. [21] is used. Following Huynh [12], the Frobenius norm in the above expression can be replaced by the 2-norm, and after some manipulation, the misalignment equals

$$d = \min_{(hkl)\in\{hkl\}} \|\boldsymbol{n}(\varphi, \psi) - \boldsymbol{n}((hkl), \boldsymbol{Q})\|. \tag{88}$$

As a simple approximation, all crystallites with misalignment below a threshold value $d_{\max}$ are considered to be involved in diffraction. The higher $d_{\max}$ is chosen, the smoother and flatter simulated D-vs-$\sin^2(\psi)$ curves appear, with the maximal value $d_{\max} = 2$ containing all grains regardless of orientation, which results in a constant curve. Very low threshold values eventually prohibit a measurement, as no crystallites can be found which are aligned correctly. For the following results, $d_{\max} = 0.05$ has been chosen as a compromise.

5.3 Resolution Study

The generated microstructure volume elements consist of 10,000 grains, which corresponds to experimental conditions with particularly fine-grained samples. As the overall polycrystal is assumed to be texture-free and therefore statistically isotropic, an observed effective anisotropy would be a sign of a nonrepresentative generated microstructure volume element. The anisotropy is therefore a lower bound estimate of the total error on results for effective quantities. After numerically calculating the effective stiffness $\bar{\mathbb{C}}$, the total effective anisotropy can be quantified as the difference to the isotropic projection $\bar{\mathbb{C}}^{\mathrm{I}}$ of the effective stiffness, yielding the anisotropic error

$$e_{\text{aniso}} = \frac{\|\bar{\mathbb{C}} - \bar{\mathbb{C}}^{\mathrm{I}}\|}{\|\bar{\mathbb{C}}\|}. \tag{89}$$

For an ensemble of ten microstructures of 10,000 grains each, the anisotropic error was found to be at a mean 0.17% with standard deviation of 0.04%. As this error was found to be constant for resolutions ranging from 32^3 to 256^3 voxels, it is considered to be a representativeness error arising from the finite number of grains. Whether the degree of isotropy reached for calculation of effective stiffnesses is also sufficient of diffraction simulations will be discussed using concrete examples in subsequent sections.

The influence of the resolution on the determination of DECs was determined via a resolution study. To this end, a single microstructure of 10,000 grains was discretized with resolutions ranging from 32 voxels per side to 256 voxels per side. This corresponds to roughly 3 voxels per grain at the lower end to 1677 voxels per grain at the higher end. Between the lowest and highest resolution considered, the effective shear modulus differs on the order of 10 MPa or roughly 0.02%. However, the effect of low resolutions on DECs is significantly higher. In Fig. 5, simulated DECs for the {400} plane of pure copper are plotted for various resolutions of the same microstructure. From the highest to the lowest value, relative differences of roughly 1% are observed. As both DECs show a clear pattern of convergence, the high-resolution microstructures with 256 voxels per side depicted in Fig. 6 are used for all simulations shown in the following.

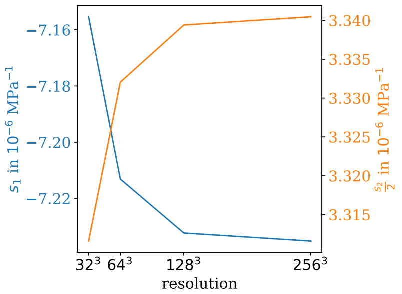

Fig. 5 DECs for the {400} plane based on different resolutions of the same copper microstructure

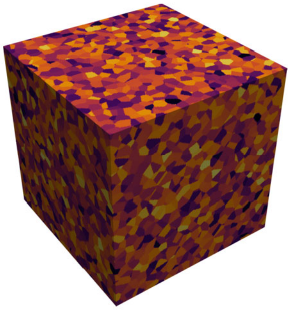

Fig. 6 Microstructure used for full-field simulations at a resolution of 256^3

6 DECs of Fine-Grained Steel

6.1 Experimental Determination of DECs

To validate the various methods of DEC calculation, an experimental determination of DECs was carried out for the body centered cubic phase of the fine grained ferritic construction steel S355MC using 4-point-bending to define a uniaxial loading. Prior to XRD stress analysis, an electrochemical layer removal of approximately 10 μm was carried out to remove effects induced in the near-surface region by previous manufacturing steps.

To make sure that the results are not affected by the residual stresses that might be present due to previous manufacturing steps and plastic deformations, the loading was done with the highest loading step first. In this first load step, the sample was subjected to a unidirectional load stress of 320 MPa, corresponding to 70% of the yield strength R_{eH}. Subsequently, the sample was unloaded in four steps.

XRD stress analysis was carried out according to the $\sin^2\psi$ method on the {211}-lattice planes of the ferrite phase using CrKa-radiation. A bending device built in-house was used to apply the loading, allowing for sample tilts for measurements in loading direction up to 60°. 21 sample tilts were applied in the region $-60° \leq \psi \leq 60°$, equidistantly distributed in $\sin^2\psi$. As primary aperture, a pinhole collimator with a nominal diameter of 1 mm was applied. On the secondary beam path a $2\theta = 0.4°$ slit aperture was used in front of a scintillation counter. For peak profile fitting Pearson VII functions were applied after linear background substraction.

In Fig. 7, the five resulting $\sin^2(\psi)$ plots at $\varphi = 0$ are shown along with linear regression plots of the same. The intersection of all five linear regressions yields the lattice plane distance of the strain-independent direction $D^* = 1.17015$ Å, which is assumed to equal D_0. In Fig. 8, the intercepts and slopes of the linear regression plots from Fig. 7 are plotted against

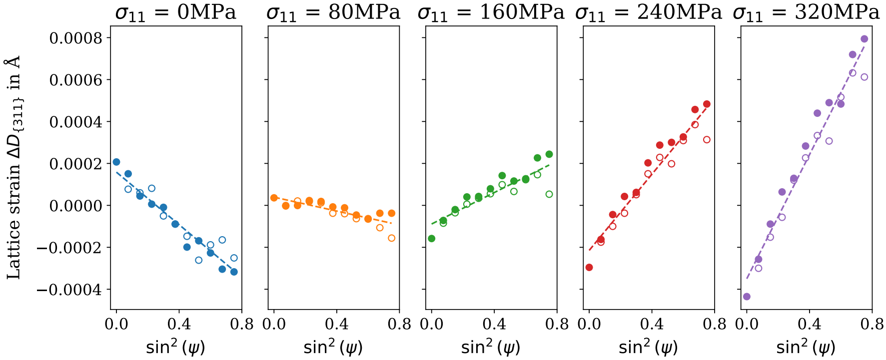

Fig. 7 $\sin^2(\psi)$ plots of uniaxially loaded S355MC samples in the $\{211\}$ lattice plane at $\varphi = 0$

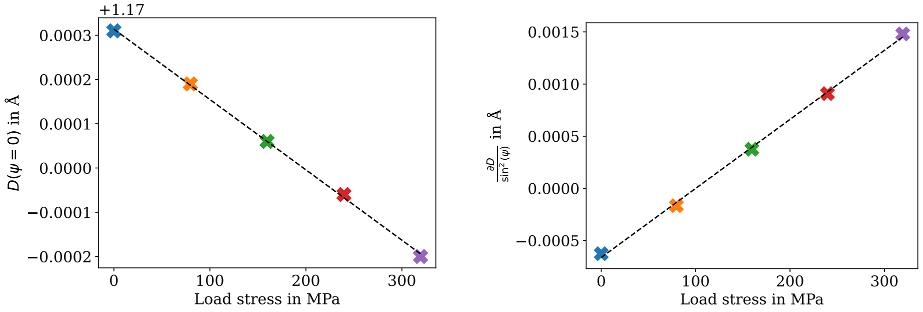

(a) Axis intercepts and least-square fit

(b) Slopes and least-square fit

Fig. 8 Axis intercepts and slopes of D-vs-$\sin^2(\psi)$ curves shown in Fig. 7. From the slope of both plots the diffraction elastic constants s_1 and ½s_2 can be derived

the applied load stress. A linear regression for these intercepts and slopes yields DEC values of

$$s_1 = -1.36 \times 10^{-6}\ \mathrm{MPa}^{-1}, \tag{90}$$

$$\frac{s_2}{2} = 5.655 \times 10^{-6}\ \mathrm{MPa}^{-1}. \tag{91}$$

The deviation of measurement points from the linear regression implies standard deviations of the DEC values of

$$\mathrm{std}(s_1) = 1.173 \times 10^{-7}\ \mathrm{MPa}^{-1}, \tag{92}$$

$$\mathrm{std}\left(\frac{s_2}{2}\right) = 1.632 \times 10^{-8}\ \mathrm{MPa}^{-1}. \tag{93}$$

These standard deviations do not include potential errors due to texture, stress gradients or other violations of the core assumptions.

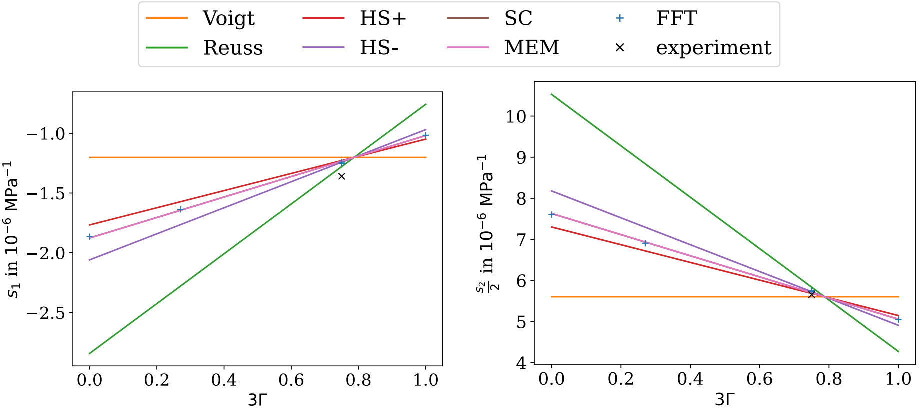

(a) s_1 diffraction elastic constant (b) ½s_2 diffraction elastic constant

Fig. 9 DECs plotted against the lattice plane parameter 3Γ for the ferritic steel S355MC

6.2 Comparison of Experimental, Numerical and Theoretical DEC

In Fig. 9, experimental, numerical and theoretical values for the DECs of the ferritic steel S355MC are plotted against the lattice plane parameter 3Γ. For S355MC, we assume single crystal elastic constants equal to pure iron, which are

$$C_{1111} = 230 \text{ GPa}, \quad C_{1122} = 135 \text{ GPa}, \quad C_{1212} = 117 \text{ GPa}, \tag{94}$$

according to Landolt-Börnstein [6]. As discussed in Sect. 3, the Voigt and Reuss approaches form relatively wide bounds on the theoretically possible values of the DECs, while the Hashin-Shtrikman bounds are considerably tighter. The self-consistent method falls between the Hashin-Shtrikman bounds.

For the values of the MEM shown in the diagram, an effective shear modulus of $\bar{G} = 82.15$ GPa is used which was calculated via numerical homogenization using the same methodology as the full-field simulations. As the effective shear modulus given by the self-consistent method yields the same value to within four significant digits, the MEM and the self-consistent method are indistinguishable in the diagram.

From simulated D-vs-$\sin^2(\psi)$ curves, slopes and intercepts were obtained via linear regression for each of the {200}, {310}, {211}, and {222} lattice planes. Since in the simulated setting the stress is known exactly, simulated DECs can be calculated directly from those slopes and intercepts. The simulated DECs are very close to the theoretical results obtained via the MEM and self-consistent method. However, unlike theoretical predictions, they do not lie exactly on a straight line. This slight deviation could be explained by the slight anisotropy present in the 10,000 grain representative volume element. While the effect of nonrepresentative on effective elastic constants was found to be on the order of 0.1%, simulated DECs could be more sensitive to nonrepresentative anisotropy, just as simulated DECs are more sensitive to numerical errors due to low resolutions. Regardless, the deviation of the simulated DECs from a theoretical straight line is small compared to the deviations between different methods.

The experimental results violate theoretical bounds. The experimentally determined value of s_1 lies outside the Voigt-Reuss bounds by roughly 0.1×10^{-6} MPa^{-1}, which amounts to roughly the difference spanned by the Voigt-Reuss bounds for the same value of 3Γ. A likely reason for this deviation between experiment and theory is the use of pure iron single crystal elastic constants for S355MC. Another possible factor is that the theoretical model neglects the presence of cementite present in the pearlite phase, which could however not fully explain a violation of Voigt-Reuss bounds due to the low volume fraction of cementite in the low-carbon steel. The influence of texture was ruled out based on texture measurements, and the influence of residual stress gradients is unlikely to be significant due to the small X-ray penetration depth. Deviations from the assumed plane stress state could not explain a violation of the Voigt-Reuss bounds. We conclude that the deviations in s_1 are most likely explained by the use of pure iron single crystal elastic constants, along with the general measurement uncertainty.

Stress analysis using the $\sin^2(\psi)$ technique uses ½s_2, the experimentally determined value of which lies between the Voigt-Reuss bounds. It violates the second-order Hashin-Shtrikman bounds, which, aside from the previously discussed sources of error, might simply be explained by the microstructure not corresponding to the Hashin-Shtrikman assumption of a spherical two-point statistic.

The observed violation of the bounds, while large in relative terms, is small in terms of the absolute values of s_1 and ½s_2, and thus would have only a small effect on stress analysis using the DECs. As shown in Fig. 9, the ½s_2-values of the Voigt and Reuss bounds are close for the measured {211} plane, while for the {200}, the values differ strongly. As a consequence, for the {211} plane, stress analysis is not particularly sensitive to the choice of the micromechanical model. In the following section, the influence of deviations in DECs on the stress analysis is quantified for measurements in the more sensitive {200} plane of a different material.

7 Stress Analysis of Pure Copper

As an example in which stress analysis is particularly sensitive with regards to the DECs, we conduct a stress analysis of pure copper for the {400} plane. In Fig. 10, predicted lattice normal strains are plotted against $\sin^2(\psi)$ for a known stress state of $\sigma_{11} = 100$ MPa and $\sigma_{22} = 100$ MPa. The results are similar to those obtained in the previous section, in that the numerical results respect the Hashin-Shtrikman bounds and are in good agreement with the MEM and the self-consistent method. The numerical results show a very slight stochastic deviation from a perfect line, which is again presumed to be due to the finite simulated volume being slightly nonrepresentative of a statistically isotropic microstructure.

While Fig. 10 illustrates theoretical approaches to predict lattice normal strains, XRD stress analysis requires a solution of the inverse problem, i.e., recovering the effective stress from experimentally determined lattice plane distance values. To avoid sources of error induced by experimental uncertainties, numerical simulations are used as a source of distance values in this section. The approach is based on a commonly used experimental technique; see, e.g., Dölle and Hauk [4]. Simulated diffraction experiments in the {400} lattice plane are performed at three azimuth angles $\varphi \in \{0, \pi/4, \pi/2\}$. The slope of the $\sin^2(\psi)$-plots equals

$$\frac{\partial \boldsymbol{\varepsilon} \cdot (\boldsymbol{n} \otimes \boldsymbol{n})}{\partial \sin^2(\psi)} = \frac{s_2}{2}(\bar{\sigma}_{11}\cos^2(\varphi) + \bar{\sigma}_{12}\sin(2\varphi) + \bar{\sigma}_{22}\sin^2(\varphi)). \tag{95}$$

Simulated measurements of the slope for three azimuth angles φ are sufficient to determine the three components of a planar effective stress for any given ½s_2.

Fig. 10 Predicted $\sin^2(\psi)$ results for pure copper with $\varphi = 0$ for the $\{400\}$ lattice plane

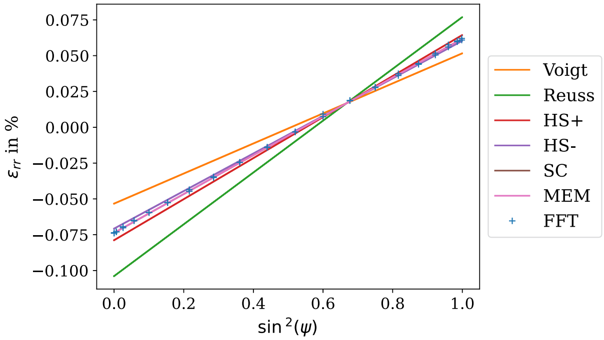

Table 1 Effective shear modulus and stress measurements according to various methods

	FFT	Reuss	HS−	MEM	SC	HS+	Voigt
$\bar{G}$ (GPa)	44.8	41.15	44.13	44.8	44.8	45.19	47.66
σ_{11} (MPa)	100	75.36	95.15	100.5	100.51	103.96	129.9
σ_{22} (MPa)	100	77.04	97.26	102.73	102.74	106.26	132.79
σ_{12} (MPa)	0	−1.36	−1.72	−1.82	−1.82	−1.88	−2.35
e_σ (%)	0	23.83	4.12	2.35	2.35	5.4	31.42

For simulated diffraction measurements, the effective stress applied in the simulation is the reference to which analysis results must be compared. The stress $\boldsymbol{\sigma}$ resulting from the above calculation therefore has a total relative error of

$$e_\sigma = \frac{\|\boldsymbol{\sigma} - \boldsymbol{\sigma}_{\mathrm{FFT}}\|}{\|\boldsymbol{\sigma}_{\mathrm{FFT}}\|}. \tag{96}$$

In Table 1, results for analytically calculated DEC are shown. For measurements for the $\{400\}$ lattice plane, XRD stress analysis is highly sensitive to the choice of analytical approximation. In the case of the Voigt approximation, a relative error of 6.4% in the effective shear modulus is associated with a stress analysis error of 31.38%. An accurate estimate of the effective shear modulus is associated with a low stress analysis error. As in all other examples shown in this paper, the self-consistent method is very close to the simulated effective stiffness. The MEM, using the exact simulated effective shear modulus, yields only slightly improved results. As the difference between MEM and self-consistent results is smaller than the numerical error, both methods should be considered equally well-suited for the material and microstructure considered, and a distinction could only be drawn with more accurate simulations. Since the self-consistent method entails a specific assumption for the microstructure, it may not perform this well for other materials or microstructures. The MEM, on the other hand, can be tailored to a given effective shear modulus. We therefore expect it to remain accurate for other texture-free microstructures if the effective shear modulus can be determined accurately, i.e., through tensile tests or other experiments.

8 Summary and Conclusions

In this work, the calculation of diffraction elastic constants (DECs) of statistically isotropic cubic polycrystals using the Maximum Entropy Method (MEM) was considered. To serve as a comparison, a classical micromechanical approach to the calculation of isotropic DECs was reduced to a one-dimensional homogenization problem parametrized by the effective shear modulus. Using the singular approximation, a general solution scheme was proposed which includes the existing Voigt, Reuss, Hashin-Shtrikman and self-consistent (Eshelby-Kröner) methods. From the perspective of practical use, this solution scheme is equivalent to a one-dimensional parametrization and interpolation using the effective shear modulus as a parameter, which allows fine-tuning of DECs based on tensile tests of the material to be measured.

As an alternative path to similar results, the MEM was applied to the problem of DEC calculation. As with the singular approximation, the MEM yields a parametrization in terms of the effective shear modulus. MEM and singular approximation results are compatible. The advantage of the MEM lies in its greater flexibility in parametrization. Unlike classical Eshelby approaches, which rely on microstructural assumptions for the interaction between crystallites, the MEM incorporates microstructural coupling assumptions indirectly through a (possibly measured) effective stiffness tensor. The application of the MEM to textured and multiphase XRD stress analysis, which has not been attempted in this work for reasons of scope, is expected to be straightforward based on the existing MEM formulas for textured and multiphase cases as described in Krause and Böhlke [15].

To validate the derived methods, simulations of X-ray diffraction (XRD) stress analyses were carried out. An FFT-based solver was used to calculate full-field stress and strain information of computationally generated polycrystalline microstructures with large numbers of grains. Both in terms of simulated diffraction measurements and effective shear modulus, the self-consistent method happened to yield very accurate results for the material considered. Using the MEM with the effective shear modulus from a computational homogenization of the same microstructure resulted in stress analyses with a similar accuracy. In the context of the numerical precision of the simulations used, the accuracy of the MEM and the self-consistent method cannot be meaningfully distinguished. Other established methods such as Voigt, Reuss and Hashin-Shtrikman approaches predicted inaccurate effective shear moduli and yielded inaccurate results when applied to stress analysis based on diffraction measurements for the material states considered in this work. The error in stress calculation was found to be far larger than the error in shear modulus prediction, highlighting the importance of accurate models even for materials for which tight bounds on the effective stiffness can be established.

In conclusion, the MEM was evaluated for statistically isotropic cubic polycrystals and found to be in agreement with classic micromechanical approaches available for this special case. Advantages of the MEM lie in its straightforward and explicit analytical formulation compared to classical approaches which require numerical solution of integrals and nonlinear equations for more complicated materials. Additionally, the MEM does not rely on explicit microstructural symmetry assumptions and can be adapted to selectively incorporate information about the considered material such as macroscopic stiffness measurements. Further work oriented towards application of the MEM to textured materials and experimental results is forthcoming.

Appendix A: Calculation of Cubic Strain Concentration Tensors

If, for a statistically isotropic cubic polycrystal, $\mathbb{A}(\boldsymbol{Q}) = \boldsymbol{Q} \star \mathbb{A}_0$, $\mathbb{A}(\boldsymbol{Q})$ is fully determined by $\bar{G}$, as will be shown in the following. By taking the volume average of the definition of the strain concentration tensor in Equation (21),

$$\langle \mathbb{A} \rangle = \mathbb{I}^{\mathrm{S}}. \tag{97}$$

With the cubic projector decomposition of $\mathbb{A}_0$ and the projection relation Equation (28),

$$\lambda_1^{\mathrm{A}} \mathbb{P}^{\circ} + \left(\frac{2}{5} \lambda_2^{\mathrm{A}} + \frac{3}{5} \lambda_3^{\mathrm{A}} \right) \mathbb{P}' = \mathbb{I}^{\mathrm{S}} = \mathbb{P}^{\circ} + \mathbb{P}'. \tag{98}$$

From the spherical part, $\lambda_1^{\mathrm{A}} = 1$, from which it follows that spherical strains are homogeneous. The deviatoric part leads to

$$\frac{2}{5} \lambda_2^{\mathrm{A}} + \frac{3}{5} \lambda_3^{\mathrm{A}} = 1. \tag{99}$$

Similarly, the definition of effective stress leads from

$$\langle \mathbb{C} \mathbb{A} \rangle = \bar{\mathbb{C}} \tag{100}$$

via the projector decompositions of $\mathbb{A}_0$ and $\mathbb{C}_0$ to

$$\lambda_1^{\mathrm{C}} \lambda_1^{\mathrm{A}} \mathbb{P}^{\circ} + \left(\frac{2}{5} \lambda_2^{\mathrm{C}} \lambda_2^{\mathrm{A}} + \frac{3}{5} \lambda_3^{\mathrm{C}} \lambda_3^{\mathrm{A}} \right) \mathbb{P}' = 3 \bar{K} \mathbb{P}^{\circ} + 2 \bar{G} \mathbb{P}'. \tag{101}$$

From the spherical part follows the effective compression modulus. The deviatoric part resolves to

$$\frac{2}{5} \lambda_2^{\mathrm{C}} \lambda_2^{\mathrm{A}} + \frac{3}{5} \lambda_3^{\mathrm{C}} \lambda_3^{\mathrm{A}} = 2 \bar{G}. \tag{102}$$

Solving Equation (99) and Equation (102) for λ^{A} yields

$$\lambda_2^{\mathrm{A}} = \frac{-5 \lambda_3^{\mathrm{C}} + 10 \bar{G}}{2 \lambda_2^{\mathrm{C}} - 2 \lambda_3^{\mathrm{C}}}, \tag{103}$$

$$\lambda_3^{\mathrm{A}} = \frac{5 \lambda_2^{\mathrm{C}} - 10 \bar{G}}{3 \lambda_2^{\mathrm{C}} - 3 \lambda_3^{\mathrm{C}}}. \tag{104}$$

Appendix B: Calculation of Stress Factors

As in Sect. 2.2.1, $\mathbb{A}(\boldsymbol{Q}) = \boldsymbol{Q} \star \mathbb{A}_0$ is assumed. The calculation of stress factors requires the term

$$\langle \mathbb{A}^{\mathsf{TH}} \rangle_g [\boldsymbol{n} \otimes \boldsymbol{n}] = \langle \boldsymbol{Q} \star \left(\mathbb{P}^{\circ} + \lambda_2^{\mathrm{A}} \mathbb{P}_2^{\mathrm{C}} + \lambda_3^{\mathrm{A}} \mathbb{P}_3^{\mathrm{C}} \right) \rangle_g [\boldsymbol{n} \otimes \boldsymbol{n}]. \tag{105}$$

After separating the isotropic parts of the projectors out of the expression,

$$\begin{aligned} \langle \mathbb{A}^{\mathsf{TH}} \rangle_g [\boldsymbol{n} \otimes \boldsymbol{n}] &= \left((1 - \lambda_2^{\mathrm{A}}) \mathbb{P}^{\circ} + \lambda_3^{\mathrm{A}} \mathbb{I}^{\mathrm{S}} + (\lambda_2^{\mathrm{A}} - \lambda_3^{\mathrm{A}}) \langle \mathbb{D} \rangle_g \right) [\boldsymbol{n} \otimes \boldsymbol{n}] && (106) \\ &= \frac{(1 - \lambda_2^{\mathrm{A}})}{3} \boldsymbol{I} + \lambda_3^{\mathrm{A}} [\boldsymbol{n} \otimes \boldsymbol{n}] + (\lambda_2^{\mathrm{A}} - \lambda_3^{\mathrm{A}}) \langle \mathbb{D} [\boldsymbol{n} \otimes \boldsymbol{n}] \rangle_g. && (107) \end{aligned}$$

For the anisotropic parts, the crystal lattice plane (hkl) can be chosen without loss of generality, as the g-average of a cubically symmetric tensor does not change when permuting (hkl). Via the depiction of $\boldsymbol{n}$ given in Equation (3),

$$\mathbb{D}[\boldsymbol{n} \otimes \boldsymbol{n}] = \frac{h^2 \boldsymbol{g}_1 \otimes \boldsymbol{g}_1 + k^2 \boldsymbol{g}_2 \otimes \boldsymbol{g}_2 + l^2 \boldsymbol{g}_3 \otimes \boldsymbol{g}_3}{h^2 + k^2 + l^2}. \tag{108}$$

To calculate $\langle \mathbb{D}[\boldsymbol{n} \otimes \boldsymbol{n}] \rangle_g$, a symmetry argument over g can be used. Unlike the statistical average over all crystals $\langle \cdot \rangle$, $\langle \cdot \rangle_g$ is not given by an isotropic projection. Instead, g is transversally isotropic around $\boldsymbol{n}$, see Equation (6). Therefore, for a second order tensor $\boldsymbol{B} = \boldsymbol{Q} \star \boldsymbol{B}_0$, calculating $\langle \cdot \rangle_g$ is equivalent to the transversal-isotropic projection

$$\langle \boldsymbol{B} \rangle_g = (\boldsymbol{n} \cdot \boldsymbol{B}_0 \boldsymbol{n}) \, \boldsymbol{n} \otimes \boldsymbol{n} + \frac{1}{2} \left(\boldsymbol{I} \cdot \boldsymbol{B}_0 - \boldsymbol{n} \cdot \boldsymbol{B}_0 \boldsymbol{n} \right) \left(\boldsymbol{I} - \boldsymbol{n} \otimes \boldsymbol{n} \right). \tag{109}$$

Applying this transversal symmetry projection results in

$$\langle \mathbb{D}[\boldsymbol{n} \otimes \boldsymbol{n}] \rangle_g = \Gamma \boldsymbol{I} + (1 - 3\Gamma) \boldsymbol{n} \otimes \boldsymbol{n}, \tag{110}$$

with the lattice plane parameter 3Γ defined as

$$3\Gamma = 3 \frac{h^2 k^2 + h^2 l^2 + k^2 l^2}{\left(h^2 + k^2 + l^2 \right)^2}. \tag{111}$$

The stress factor $\boldsymbol{F}$ is given by

$$\begin{aligned} \boldsymbol{F} &= \bar{\mathbb{C}}^{-1}[\langle \mathbb{A}^{\mathsf{TH}} \rangle_g [\boldsymbol{n} \otimes \boldsymbol{n}]] \\ &= \left(\left(\frac{1}{3\bar{K}} - \frac{1}{3\bar{G}} \right) \mathbb{P}^{\circ} + \frac{1}{2\bar{G}} \mathbb{P}' \right) \left[\frac{1 - \lambda_2^{\mathrm{A}}}{3} \boldsymbol{I} + \lambda_3^{\mathrm{A}} [\boldsymbol{n} \otimes \boldsymbol{n}] + (\lambda_2^{\mathrm{A}} - \lambda_3^{\mathrm{A}}) \langle \mathbb{D}[\boldsymbol{n} \otimes \boldsymbol{n}] \rangle_g \right]. \end{aligned} \tag{112}$$

With the parametrization by $\bar{G}$ given in Appendix A,

$$\begin{aligned} \boldsymbol{F} = &\frac{-5\lambda_1^{\mathrm{C}} \left(2\Gamma \lambda_2^{\mathrm{C}} + 3\Gamma \lambda_3^{\mathrm{C}} - 10\Gamma \bar{G} - \lambda_3^{\mathrm{C}} + 2\bar{G} \right) + 4\bar{G} \left(\lambda_2^{\mathrm{C}} - \lambda_3^{\mathrm{C}} \right)}{12 \lambda_1^{\mathrm{C}} \bar{G} \left(\lambda_2^{\mathrm{C}} - \lambda_3^{\mathrm{C}} \right)} \boldsymbol{I} \\ &+ \frac{5 \left(2\Gamma \lambda_2^{\mathrm{C}} + 3\Gamma \lambda_3^{\mathrm{C}} - 10\Gamma \bar{G} - \lambda_3^{\mathrm{C}} + 2\bar{G} \right)}{4\bar{G} \left(\lambda_2^{\mathrm{C}} - \lambda_3^{\mathrm{C}} \right)} (\boldsymbol{n} \otimes \boldsymbol{n}). \end{aligned} \tag{113}$$

Appendix C: Maximum Entropy Method

In the following, the derivation of the analytical solution of maximum entropy will be summarized for the case of linear elastic polycrystals without stress-free strains. In that case, the probability distribution to be solved for is $p(\boldsymbol{\varepsilon}, \boldsymbol{Q})$. The entropy functional follows as

$$S = -\iint p(\boldsymbol{\varepsilon}, \boldsymbol{Q}) \ln(p(\boldsymbol{\varepsilon}, \boldsymbol{Q})) \, \mathrm{d}\boldsymbol{\varepsilon} \, \mathrm{d}\boldsymbol{Q}. \tag{114}$$

The maximization of that functional involves constraints given by what is known about the material and the loading,

$$\langle \boldsymbol{\varepsilon} \rangle = \bar{\boldsymbol{\varepsilon}}, \qquad \langle (\boldsymbol{Q} \star \mathbb{C}_0)[\boldsymbol{\varepsilon}] \rangle = \bar{\mathbb{C}}[\bar{\boldsymbol{\varepsilon}}], \tag{115}$$

$$\langle \boldsymbol{\varepsilon} \cdot (\boldsymbol{Q} \star \mathbb{C}_0)[\boldsymbol{\varepsilon}] \rangle = \bar{\boldsymbol{\varepsilon}} \cdot \bar{\mathbb{C}}[\bar{\boldsymbol{\varepsilon}}], \qquad \int p(\boldsymbol{\varepsilon}, \boldsymbol{Q}) \,\mathrm{d}\boldsymbol{\varepsilon} = f(\boldsymbol{Q}), \tag{116}$$

where $f(\boldsymbol{Q})$ is the orientation distribution function, which is 1 for statistically isotropic polycrystals.

The right-hand sides of the constraints can be neglected in the following, as they do not contribute after differentiation of the functional. After a scalar product with a Lagrange multiplier from the vector space corresponding to each constraint, the constraints are added to the entropy functional, resulting in the modified entropy functional

$$\begin{aligned} S_{\mathrm{mod}} = \iint & p(\boldsymbol{\varepsilon}, \boldsymbol{Q})(-\ln(p(\boldsymbol{\varepsilon}, \mathbb{C})) + \boldsymbol{\lambda}_{\varepsilon} \cdot \boldsymbol{\varepsilon} + \boldsymbol{\lambda}_{\sigma} \cdot \boldsymbol{\sigma} \\ & + \lambda_w \boldsymbol{\varepsilon} \cdot (\boldsymbol{Q} \star \mathbb{C}_0)[\boldsymbol{\varepsilon}] + \lambda_Q(\boldsymbol{Q})) \,\mathrm{d}\boldsymbol{\varepsilon} \,\mathrm{d}\boldsymbol{Q}. \end{aligned} \tag{117}$$

The optimization of the functional can then be rephrased as a partial differentiation of the integrand by p, leading to

$$\ln(p(\boldsymbol{\varepsilon}, \boldsymbol{Q})) = -1 + \boldsymbol{\lambda}_{\varepsilon} \cdot \boldsymbol{\varepsilon} + \boldsymbol{\lambda}_{\sigma} \cdot \boldsymbol{\sigma} + \lambda_w \boldsymbol{\varepsilon} \cdot (\boldsymbol{Q} \star \mathbb{C}_0)[\boldsymbol{\varepsilon}] + \lambda_Q(\boldsymbol{Q})$$

such that

$$p(\boldsymbol{\varepsilon}, \boldsymbol{Q}) = \exp(-1 + \boldsymbol{\lambda}_{\varepsilon} \cdot \boldsymbol{\varepsilon} + \boldsymbol{\lambda}_{\sigma} \cdot \boldsymbol{\sigma} + \lambda_w \cdot (\boldsymbol{Q} \star \mathbb{C}_0) + \lambda_Q(\boldsymbol{Q})).$$

Substitution of the Lagrange multipliers with $\boldsymbol{\gamma} = (\boldsymbol{Q} \star \mathbb{C}_0^{-1})[\boldsymbol{\mu}_{\varepsilon}] + \boldsymbol{\mu}_{\sigma}$ and d leads to a more recognizable normal distribution

$$p(\boldsymbol{\varepsilon}, \boldsymbol{Q}) = m(\boldsymbol{Q}) \exp\left(\frac{1}{2} d(\boldsymbol{\varepsilon} - \boldsymbol{\gamma}) \cdot (\boldsymbol{Q} \star \mathbb{C}_0^{-1})[\boldsymbol{\varepsilon} - \boldsymbol{\gamma}]\right), \tag{118}$$

where $m(\boldsymbol{Q})$ contains various expressions which do not depend on $\boldsymbol{\varepsilon}$. The function $m(\boldsymbol{Q})$ and the variables $\boldsymbol{\mu}_{\sigma}$, $\boldsymbol{\mu}_{\varepsilon}$ and d are then determined by evaluating the constraints for this probability distribution, resulting in the formulas given in Sect. 4.

Author contributions Conceptualization, M.K.; Methodology, M.K.; Software, M.K.; Validation, M.K.; Formal Analysis, M.K.; Investigation, M.Z. and M.K.; Resources, J.G. and T.B.; Data Curation, M.K.; Writing–Original Draft, M.K.; Writing–Review & Editing, M.K., M.Z., J.G. and T.B.; Visualization, M.K.; Supervision, T.B.; Project Administration, T.B.; Funding Acquisition, T.B.

Funding Open Access funding enabled and organized by Projekt DEAL. The research documented in this paper was funded (BO 1466/14-1 and GI376/28-1) by the German Research Foundation (DFG) as part of project 512640977, 'Evaluation of non-linear $\sin^2 \psi$ - distributions in residual stress analysis based on a scale-bridging mechanical modeling'. The support by the German Research Foundation (DFG) is gratefully acknowledged.

Data Availability No datasets were generated or analysed during the current study.

Declarations

Competing interests The authors declare no competing interests.

References

1. Behnken, H., Hauk, V.: Berechnung der röntgenographischen Spannungsfaktoren texturierter Werkstoffe-Vergleich mit experimentellen Ergebnissen/Calculation of X-ray stress factors of textured materials-comparison with experimental results. Int. J. Mater. Res. **82**(2), 151–158 (1991)
2. Böhlke, T., Jöchen, K., Kraft, O., Löhe, D., Schulze, V.: Elastic properties of polycrystalline microcomponents. Mech. Mater. **42**(1), 11–23 (2010)
3. Bollenrath, F., Hauk, V., Müller, E.H.: Zur Berechnung der vielkristallinen Elastizitätskonstanten aus den Werten der Einkristalle. Int. J. Mater. Res. **58**(1), 76–82 (1967)
4. Dölle, H., Hauk, V.: Röntgenographische Spannungsermittlung für Eigenspannungssysteme allgemeiner Orientierung. J. Heat Treat. Mater. **31**(3), 165–168 (1976)
5. Eshelby, J.D.: The determination of the elastic field of an ellipsoidal inclusion, and related problems. Proc. R. Soc. **247**, 376–396 (1957)
6. Every, A., McCurdy, A.: Second and higher order elastic constants. Landolt-Börnstein Numerical Data and Functional Relationships in Science and Technology New Series Group III: Crystal and Solid State Physics **29**, 743 (1992)
7. Fokin, A.: Solution of statistical problems in elasticity theory in the singular approximation. J. Appl. Mech. Tech. Phys. **13**(1), 85–89 (1972)
8. Frigo, M., Johnson, S.G.: The design and implementation of FFTW3. Proc. IEEE **93**(2), 216–231 (2005)
9. Gehrig, F., Wicht, D., Krause, M., Böhlke, T.: FFT-based investigation of the shear stress distribution in face-centered cubic polycrystals. Int. J. Plast. **157**, 103369 (2022)
10. Guo, J., Fu, H., Pan, B., Kang, R.: Recent progress of residual stress measurement methods: a review. Chin. J. Aeronaut. **34**(2), 54–78 (2021)
11. Hill, R.: Elastic properties of reinforced solids: some theoretical principles. J. Mech. Phys. Solids **11**(5), 357–372 (1963)
12. Huynh, D.Q.: Metrics for 3d rotations: comparison and analysis. J. Math. Imaging Vis. **35**(2), 155–164 (2009)
13. Jaynes, E.T.: Statistical Physics. Brandeis Summer Institute Lectures in Theoretical Physics., vol. 3. W.A. Benjamin Inc., New York (1963)
14. Kocks, U.F., Tomé, C.N., Wenk, H.-R.: Texture and Anisotropy. Cambridge University Press, Cambridge (1998)
15. Krause, M., Böhlke, T.: Maximum-entropy based estimates of stress and strain in thermoelastic random heterogeneous materials. J. Elast. **141**, 321–348 (2020)
16. Krause, M., Böhlke, T.: in print. Tensorial harmonic bases of arbitrary order with applications in elasticity, elastoviscoplasticity and texture-based modeling. Math. Mech. Solids.
17. Kreher, W., Pompe, W.: Field fluctuations in a heterogeneous elastic material–an information theory approach. J. Mech. Phys. Solids **33**(5), 419–445 (1985)
18. Kreher, W., Pompe, W.: Internal Stresses in Heterogeneous Solids. Physical Research., vol. 9. Akademie-Verlag, Berlin (1989)
19. Kröner, E.: Berechnung der elastischen Konstanten des Vielkristalls aus den Konstanten des Einkristalls. Z. Phys. **151**(4), 504–518 (1958)
20. Kuhn, J., Schneider, M., Sonnweber-Ribic, P., Böhlke, T.: Generating polycrystalline microstructures with prescribed tensorial texture coefficients. Comput. Mech. **70**(3), 639–659 (2022)
21. Larochelle, P.M., Murray, A.P., Angeles, J.: A distance metric for finite sets of rigid-body displacements via the polar decomposition. J. Mech. Des. **129**(8), 883–886 (2006)
22. Lester, H., Aborn, R.: Behavior under stress of the iron crystals. Army Ordnance **6**, 1926 (1925)
23. Lobos, M., Böhlke, T.: On optimal zeroth-order bounds of linear elastic properties of multiphase materials and application in materials design. Int. J. Solids Struct. **84**, 40–48 (2016)
24. Macherauch, E., Müller, P.: Das $\sin^2\psi$-Verfahren der röntgenographischen Spannungsmessung. Z. Angew. Phys. **13**, 305–312 (1961)

25. Moulinec, H., Suquet, P.: A numerical method for computing the overall response of nonlinear composites with complex microstructure. Comput. Methods Appl. Mech. Eng. (1998)
26. Nadeau, J.C., Ferrari, M.: On optimal zeroth-order bounds with application to Hashin-Shtrikman bounds and anisotropy parameters. Int. J. Solids Struct. **38**(44–45), 7945–7965 (2001)
27. Noyan, I.C., Cohen, J.B.: Residual Stress: Measurement by Diffraction and Interpretation. Springer, Berlin (1987)
28. Reuss, A.: Berechnung der Fließgrenze von Mischkristallen auf Grund der Plastizitätsbedingung für Einkristalle. Z. Angew. Math. Mech. **9**(1), 49–58 (1929)
29. Schneider, M., Ospald, F., Kabel, M.: Computational homogenization of elasticity on a staggered grid. Int. J. Numer. Methods Eng. **109**, 693–720 (2016)
30. Simmons, G., Wang, H.: Single Crystal Elastic Constants and Calculated Aggregate Properties: A Handbook. MIT Press, Cambridge (1971)
31. Taira, S., Tanaka, K.: Local residual stress near fatigue crack tip. Trans. Iron Steel Inst. Jpn. **19**(7), 411–418 (1979)
32. Torquato, S.: Random Heterogeneous Materials. Springer, New York (2002)
33. Voigt, W.: Ueber die Beziehung zwischen den beiden Elasticitätsconstanten isotroper Körper. Ann. Phys. **274**(12), 573–587 (1889)
34. Walpole, L.J.: On bounds for the overall elastic moduli of inhomogeneous systems-I. J. Mech. Phys. Solids **14**(3), 151–162 (1966)
35. Wicht, D., Schneider, M., Böhlke, T.: An efficient solution scheme for small-strain crystal-elasto-viscoplasticity in a dual framework. Comput. Methods Appl. Mech. Eng. **358**, 112611 (2020)
36. Wicht, D., Schneider, M., Böhlke, T.: On quasi-Newton methods in fast Fourier transform-based micromechanics. Int. J. Numer. Methods Eng. **121**(8), 1665–1694 (2020)
37. Willis, J.R.: Bounds and self-consistent estimates for the overall properties of anisotropic composites. J. Mech. Phys. Solids **25**(3), 185–202 (1977)
38. Willis, J.R.: Variational and related methods for the overall properties of composites. Adv. Appl. Mech. **21**, 1–78 (1981)
39. Zeman, J., Vondřejc, J., Novák, J., Marekc, I.: Accelerating a FFT-based solver for numerical homogenization of periodic media by conjugate gradients. J. Comput. Phys. **229**, 8065–8071 (2010)